

# Numerical study of the shock wave and pressure induced by single bubble collapse near planar solid wall

Cite as: Phys. Fluids **33**, 073311 (2021); <https://doi.org/10.1063/5.0055727>

Submitted: 02 May 2021 . Accepted: 19 June 2021 . Published Online: 16 July 2021

Xiaobin Yang (杨晓彬),  Cheng Liu (刘成),  Decheng Wan (万德成), and  Changhong Hu (胡长洪)



View Online



Export Citation



CrossMark

## ARTICLES YOU MAY BE INTERESTED IN

[A modified Oldroyd-B model for non-colloidal suspensions](#)

Physics of Fluids **33**, 073105 (2021); <https://doi.org/10.1063/5.0059382>

[The wobbling motion of single and two inline bubbles rising in quiescent liquid](#)

Physics of Fluids **33**, 073305 (2021); <https://doi.org/10.1063/5.0055804>

[Unsteady flow structures behind a shark denticle replica on the wall: Time-resolved particle image velocimetry measurements](#)

Physics of Fluids **33**, 075109 (2021); <https://doi.org/10.1063/5.0057699>

Physics of Fluids

SPECIAL TOPIC: Flow and Acoustics of Unmanned Vehicles

Submit Today!



# Numerical study of the shock wave and pressure induced by single bubble collapse near planar solid wall

Cite as: Phys. Fluids **33**, 073311 (2021); doi: 10.1063/5.0055727

Submitted: 2 May 2021 · Accepted: 19 June 2021 ·

Published Online: 16 July 2021



View Online



Export Citation



CrossMark

Xiaobin Yang (杨晓彬),<sup>1,a)</sup> Cheng Liu (刘成),<sup>1,a)</sup>  Decheng Wan (万德成),<sup>1</sup>  and Changhong Hu (胡长洪)<sup>2</sup> 

## AFFILIATIONS

<sup>1</sup>Computational Marine Hydrodynamic Lab (CMHL), School of Naval Architecture, Ocean and Civil Engineering, Shanghai Jiao Tong University, Shanghai 200240, China

<sup>2</sup>Research Institute for Applied Mechanics, Kyushu University, Fukuoka 816-0811, Japan

<sup>a)</sup>Author to whom correspondence should be addressed: [chengliu@sjtu.edu.cn](mailto:chengliu@sjtu.edu.cn)

## ABSTRACT

Bubble collapse is one of the leading causes for the cavitation erosion of submerged structures. For better understanding of the destructive mechanism of cavitation, high-fidelity simulation is performed to simulate the complete process of single bubble collapse near a planar solid wall. The wave propagation method with the approximate Riemann solver Harten Lax and van Leer Contact is adopted to solve the compressible two-phase five-equation model. We implement fifth-order weighted essentially non-oscillatory scheme with the block-structured adaptive mesh method to resolve shock waves and moving interface with high-resolution. We simulate single bubble collapsing in free-field to validate the present numerical methods and solver. Our results (e.g., averaged bubble-interior pressure and the radius variation) are found in excellent agreement with the theoretical Keller–Miksis solutions. In this study, the shock wave transmitted inside the bubble and the water-hammer shock formed in the liquid are under quantitative investigation. Numerical results reveal that the interactions between the shock wave and bubble interface give rise to peak pressures of liquid phase, and the initial stand-off distances have important influence on shock wave pattern, wall peak pressure, and bubble dynamics.

Published under an exclusive license by AIP Publishing. <https://doi.org/10.1063/5.0055727>

## I. INTRODUCTION

Bubble collapse in near-wall region is commonly encountered in many industrial processes, such as ultrasonic cavitation, propeller cavitation, and underwater explosion, etc. Shock waves<sup>1,2</sup> and the re-entrant jets generated<sup>3–6</sup> from bubble collapse may cause severe structural damage. To fully understand the mechanism of bubble collapse, various experimental methods have been developed. The spark-generated<sup>5,7–12</sup> bubble and laser-induced<sup>13–18</sup> bubble techniques are the classical experimental methods for creating cavitation bubbles, and high-speed photography can be used for the visualization of the re-entrant jet and emission of shock.

Simplified theoretical models are also proposed to provide more details of density, pressure, etc., of an inertial cavitation bubble. The first theoretical method to predict a spherical bubble collapse in free-field was proposed by Rayleigh,<sup>1</sup> based on the spherical symmetry assumption of a bubble. Later, Plesset<sup>19</sup> improved Rayleigh's method by adding the viscous and surface tension effects, which is now the prominent Rayleigh–Plesset (R–P) equation. After that, numerous

improvements for the R–P equation have been proposed, in particular, Keller and Miksis<sup>20</sup> included the compressibility effects of liquid to the R–P equation and derived the well-known Keller–Miksis (K–M) equation. The solutions of the R–P equation and K–M equation have been widely used as the validation of CFD (Computational Fluid Dynamics) approaches.<sup>21–23</sup> However, when the collapse is initiated in the vicinity of a solid wall, the presence of wall boundary hinders the inward liquid flow around bubble, leading to non-spherical collapse, which cannot be effectively resolved by the aforementioned theoretical approaches.<sup>24</sup>

In addition to the theoretical and experimental methods, numerical simulations have also been extensively used to study bubble collapse. Plesset and Chapman<sup>25</sup> were the first to develop boundary integral method (BIM) for the simulation of near-wall bubble collapse. BIM assumes the fluid to be non-viscous and incompressible, which highly improves efficiency and saves computational costs. Although BIM has been widely adopted to study bubble collapse problems,<sup>26–32</sup> the propagation of shock wave in fluid phase cannot be captured, and additional models are required whenever compressibility effects

are dominating. These limitations make it difficult to capture the main flow characteristics of violent collapses. Therefore, high-fidelity simulation based on the compressible two-phase flow equations becomes more desirable. It can reproduce an experiment with abundant and quantitatively temporal and spatial information, by which the evolution of shock waves and corresponding affection can be analyzed.

The high-density ratio of two phase fluids and the strong discontinuities of the flow field make the problem complicated and bring great challenges to the simulation. Liu and Hu<sup>33</sup> took advantage of THINC (Tangent of Hyperbola for Interface Capturing)<sup>34</sup> and GFM (Ghost Fluid Method)<sup>35</sup> to simulate the collapse of an air bubble under shock in water accurately. Allaire *et al.*<sup>36</sup> proposed a robust mechanical-equilibrium five-equation model for the simulation of the interfaces between compressible two-phase flows with high-density ratio, and the shock-induced collapse was simulated. Based on Allaire *et al.*'s work,<sup>36</sup> Deng *et al.*<sup>37</sup> presented a novel low-dissipative BVD (boundary variation diminishing) scheme and simulated the three-dimensional shock–bubble interactions. The BVD scheme employs more than one reconstruction function to minimize the variations (jumps) of the reconstructed variables at cell boundaries, which can resolve discontinuities with much less numerical dissipation. Kapila *et al.*<sup>38</sup> simplified the seven-equation of Baer and Nunziato<sup>39</sup> to a thermodynamically consistent model, which is similar to the five-equation model of Allaire *et al.*,<sup>36</sup> and the only difference between them is that the volume fraction equation of Kapila *et al.*<sup>38</sup> includes a source term ( $K\nabla \cdot \mathbf{u}$ ). Schmidmayer *et al.*<sup>23</sup> compared the above two five-equation models and the six-equation model of Saurel *et al.*<sup>40</sup> in the simulation of the Rayleigh collapse, and found that the results from the model of Kapila *et al.*<sup>38</sup> and Saurel *et al.*<sup>40</sup> have good agreements with the K–M solutions, while the model of Allaire *et al.*<sup>36</sup> cannot predict the collapse time and minimum volume of the Rayleigh collapse accurately. Tiwari<sup>21</sup> reduced the Baer–Nunziato model<sup>39</sup> to a five-equation model with interface regularization terms, and the 3D bubble collapse near solid wall was tested. The interface regularization terms can keep the thermodynamically consistent and reduce the numerical diffusion at the phase interface.

In a bubble collapsing event, the high-speed re-entrant jet and shock wave are generated when the bubble is compressed; ultimately, the collapsing process is usually accomplished with extremely short period of time. Therefore, very fine spatiotemporal resolution is required to capture shock wave and flow structure accurately. Beig and Johnsen<sup>22</sup> gave a comprehensive study of the temperatures produced during a 3D bubble collapse near solid wall using more than  $900 \times 10^6$  grids. The large amount of grid makes it not very efficient for the direct simulations. In order to save the computing expense, numerous simplified methods have been proposed. Shaw and Spelt<sup>41</sup> employed the spherically symmetric compressible quasi-conservative Euler equations with GFM to investigate the shock wave emitted during bubble collapse in free-field, and 10 000 uniform grids were adopted in an 1D computational domain. Johnsen and Colonius<sup>42–44</sup> studied the shock–bubble interactions in cylindrical coordinates with azimuthal symmetry based on  $\gamma$ -based approach proposed by Shyue,<sup>45</sup> and 720 000 grids were employed in a 2D computational domain. Hsiao *et al.*<sup>46</sup> linked the BIM solver and the compressible solver to study cavitation erosion based on a stretched grid, with finest resolution of  $10 \mu\text{m}$  in a  $1 \times 1 \text{ m}$  domain. To balance the efficiency and accuracy, Tian *et al.*<sup>47</sup> employed the adaptive mesh refinement (AMR)

technique and Eulerian finite element method to investigate the effects of buoyance parameters on the bubble oscillating behaviors. Trummer *et al.*<sup>48</sup> investigated the influence of the grid resolution on the collapse dynamics and the maximum pressures distribution, and found that the grid resolution is significant for pressure peaks.

It is well known that the water-hammer shocks and re-entrant jets account for most of cavitation erosion of the structures. In the experiment of laser-induced bubble collapsing, the emissions of shock wave during bubble rebounding can be detected with a needle-type hydrophone (Johansen *et al.*<sup>49</sup>). Numerical simulation provides an alternative way to study the shock wave emissions in the expansion stage of bubble explosion (Lechner *et al.*<sup>24</sup>), based on a multiphase flow solver InterFoam, and also by Tian *et al.*<sup>50</sup> using Eulerian finite-element method. Cao *et al.*<sup>51</sup> studied shock-induced near-wall bubble collapse numerically and captured the emitted shock waves in the liquid during collapse with phenomenological model. Johnsen and Colonius<sup>44</sup> found that the precursor shock preceded the water-hammer shock in free-field shock-induced collapse; however, the precursor shock is not clearly resolved due to the numerical dissipation. Lechner *et al.*<sup>52</sup> found when a bubble collapses very close to a solid boundary, and the jet speed can reach up to  $\sim 1000 \text{ m/s}$ .

Although shock wave emissions are extensively exist in bubble collapse, few of the numerical works emphasize the formation and propagation of the shock wave system around the interface, especially for the shocks generated inside the bubble before the emission of water-hammer shocks. Moreover, due to the numerical diffusion, the shock waves might not be resolved sharply for long-timescale simulation if traditional upwind schemes are applied. To overcome these difficulties, a compressible two-phase flow solver based on the fifth-order WENO (weighted essentially non-oscillatory) scheme<sup>53</sup> is developed. One significant advance in the present simulation is the use of block-structured AMR method.<sup>33</sup> AMR allows one to capture the shock waves and other discontinuities with high resolution, and keep the compact thickness of the interface, while leaves other non-critical regions covered with coarse mesh, providing savings in both the computational time and data storage. With the above approaches, the violent oscillations of the bubble interface are captured with high resolution, the shock waves formed inside the bubble are well-resolved, and the propagation and refraction of the shocks can be investigated quantitatively; in particular, the interactions of the shock waves and the bubble interfaces are analyzed in detail. The pressure peaks on the solid wall caused by the shock waves and the re-entrant jets are also studied.

The highlight of the present study lies in the following four aspects: (1) High-resolution compressible multiphase solver based on WENO and adaptive mesh is developed to improve the computational efficiency and accuracy in simulating bubble collapse. (2) Bubble pressure and radius predicted by this solver agree well with the theoretical solutions, even for large pressure and density ratio cases. (3) Shock waves and pressure peaks inside the bubble or in the liquid are resolved with high resolution, and the shock wave generation mechanism and the interaction between shock wave and bubble interface in the whole process of collapsing are studied quantitatively. (4) Influences of the initial stand-off distances on the peak wall pressure are discussed; the primary reason for the cavitation damage is identified to be the shock wave rather than the re-entrant jet.

The paper is structured as follows. Numerical approaches are introduced in Sec. II. Numerical validations are presented in Sec. III, including the convergence study and the comparisons of the present numerical results and the semi-analytical K–M solutions<sup>20</sup> for the Rayleigh collapse. Shock waves generated in the collapse of an air bubble near solid wall are quantitatively investigated in Sec. IV A–IV C, and the wall pressure caused by shock wave and re-entrant jet are studied in Sec. IV D. Finally, some concluding remarks are drawn in Sec. V.

## II. NUMERICAL METHODS

### A. Governing equations

The governing equations of compressible two-phase flows with Kapila’s<sup>38</sup> five-equation model are given by

$$\partial \frac{(\alpha_1 \rho_1)}{\partial t} + \nabla \cdot (\alpha_1 \rho_1 \mathbf{u}) = 0, \tag{1}$$

$$\partial \frac{(\alpha_2 \rho_2)}{\partial t} + \nabla \cdot (\alpha_2 \rho_2 \mathbf{u}) = 0, \tag{2}$$

$$\frac{\partial(\rho \mathbf{u})}{\partial t} + \nabla \cdot (\rho \mathbf{u} \mathbf{u} + p) = 0, \tag{3}$$

$$\frac{\partial E}{\partial t} + \nabla \cdot ((E + p) \mathbf{u}) = 0, \tag{4}$$

$$\frac{\partial \alpha_2}{\partial t} + \mathbf{u} \cdot \nabla \alpha_2 = K \nabla \cdot \mathbf{u}, \tag{5}$$

where  $\alpha_k$  and  $\rho_k$ , denote volume fraction and density, respectively.  $k = 1$  for liquid and  $k = 2$  for gas.  $\mathbf{u}$  indicates the velocity,  $p$  is the mixture pressure, and  $E$  is the total energy. To prevent spurious oscillations, the  $K$  term in Eq. (5) is considered on the interface cells where two fluids co-exist,<sup>54</sup> and is given by

$$K = \frac{\alpha_1 \alpha_2 (\rho_1 c_1^2 - \rho_2 c_2^2)}{\alpha_1 \rho_2 c_2^2 + \alpha_2 \rho_1 c_1^2}, \tag{6}$$

where  $c_1$  and  $c_2$  denote the sound speed of each phase. To close the governing equations, the stiffened gas equation of state (SG EOS)<sup>55</sup> is adopted

$$p = (\gamma - 1) \rho e - \gamma p_\infty, \tag{7}$$

where  $\gamma$  is the ratio of specific heats,  $p_\infty$  represents the stiffness constant, and  $e$  indicates the density of internal energy. The mixing rules<sup>38</sup> for two-phase flow can be expressed as

$$\alpha_1 + \alpha_2 = 1, \tag{8}$$

$$\alpha_1 \rho_1 + \alpha_2 \rho_2 = \rho, \tag{9}$$

$$\frac{\alpha_1}{\gamma_1 - 1} + \frac{\alpha_2}{\gamma_2 - 1} = \frac{1}{\gamma - 1}, \tag{10}$$

$$\frac{\alpha_1 p_{\infty,1}}{\gamma_1 - 1} + \frac{\alpha_2 p_{\infty,2}}{\gamma_2 - 1} = \frac{p_\infty}{\gamma - 1}. \tag{11}$$

In the present study, the sound speed of the mixture flow is computed by the mixture variables<sup>56,57</sup> as

$$c^2 = \frac{\gamma(p + p_\infty)}{\rho}. \tag{12}$$

### B. Wave propagation method

The wave propagation method<sup>37,58</sup> is used to solve the conservation laws of the form in Eq. (13). By splitting the flux difference into eigenvectors of Jacobian matrix, high-resolution results can be obtained. In the wave propagation method, flux is assumed to be continuous; thus, it is not required to compute the jumps at the interface in solving the Riemann problem.<sup>59</sup> For completeness, a brief description of the wave propagation method is presented as follows. Equations (1)–(5) are rewritten as

$$\frac{\partial \mathbf{q}}{\partial t} + \mathbf{A} \frac{\partial \mathbf{q}}{\partial x} = 0, \tag{13}$$

where  $\mathbf{q}$  is a vector of conservative variables and  $\mathbf{A}$  is the flux Jacobian matrix and can be split into subvectors as

$$\mathbf{A} = \mathbf{R} \mathbf{\Lambda} \mathbf{L}, \tag{14}$$

where  $\mathbf{\Lambda}$  is the diagonal matrix composed of the eigenvalues of  $\mathbf{A}$ ,  $\mathbf{R}$  and  $\mathbf{L}$  are, respectively, the right and left eigenvector matrix corresponding to  $\mathbf{\Lambda}$ . Let  $\Delta \mathbf{q} = \mathbf{q}_r - \mathbf{q}_l$ , where  $\mathbf{q}_l$  and  $\mathbf{q}_r$  are the left and right reconstructed conservative variables at cell boundaries, which are calculated by WENO scheme.  $\Delta \mathbf{q}$  can be reformulated as

$$\begin{aligned} \Delta \mathbf{q} &= \mathbf{q}_r - \mathbf{q}_l = \mathbf{R} \mathbf{\Lambda} \Delta \mathbf{q} = (\mathbf{r}_1, \mathbf{r}_2, \dots, \mathbf{r}_n) \begin{pmatrix} \mathbf{l}_1 \\ \mathbf{l}_2 \\ \vdots \\ \mathbf{l}_n \end{pmatrix} \Delta \mathbf{q} \\ &= (\mathbf{r}_1, \mathbf{r}_2, \dots, \mathbf{r}_n) \begin{pmatrix} \mathbf{l}_1 \Delta q \\ \mathbf{l}_2 \Delta q \\ \vdots \\ \mathbf{l}_n \Delta q \end{pmatrix} = \sum_{k=1}^n \beta_k \mathbf{r}_k, \end{aligned} \tag{15}$$

where  $\mathbf{r}_k$  and  $\mathbf{l}_k$  are the left and right eigenvectors of  $\mathbf{A}$  corresponding to its eigenvalues  $\lambda_k$  and  $\beta_k = \mathbf{l}_k \cdot \Delta \mathbf{q}$ . Analogously

$$\mathbf{A} \cdot \Delta \mathbf{q} = \mathbf{R} \mathbf{\Lambda} \mathbf{L} \Delta \mathbf{q} = \sum_{k=1}^n \lambda_k \mathbf{w}_k, \tag{16}$$

where  $\mathbf{w}_k = \beta_k \mathbf{r}_k$  refer to the discontinuities (jumps) and can be expressed as

$$\begin{cases} \mathbf{w}_1 = \mathbf{q}_l^* - \mathbf{q}_l, \\ \mathbf{w}_2 = \mathbf{q}_r^* - \mathbf{q}_l^*, \\ \mathbf{w}_3 = \mathbf{q}_r - \mathbf{q}_r^*, \end{cases} \tag{17}$$

the intermediate conservative variables  $\mathbf{q}_l^*$  and  $\mathbf{q}_r^*$  can be obtained by the three-wave approximate HLLC (Harten Lax and van Leer Contact) Riemann solver.<sup>59</sup>

At the  $i^{\text{th}}$  cell, the wave propagation method constructs the Riemann discontinuities at the cell boundaries and inside the cell; then, Eq. (13) can be rewritten as

$$\begin{aligned} \frac{\partial \mathbf{q}_i}{\partial t} &= L(\mathbf{q}_i) = -\frac{1}{\Delta x} \mathbf{A} \cdot \Delta \mathbf{q}_i \\ &= -\frac{1}{\Delta x} \left( \mathbf{A}^+ \Delta \mathbf{q}_{i-\frac{1}{2}} + \mathbf{A}^- \Delta \mathbf{q}_{i+\frac{1}{2}} + \mathbf{A} \Delta \mathbf{q}_i \right), \end{aligned} \tag{18}$$

where  $\mathbf{A}^+ \Delta \mathbf{q}_{i-1/2}$  denotes the fluctuations propagating into the cell at the left face  $x_{i-1/2}$ , with the initial states of the Riemann problem  $\mathbf{q}_{i-1/2,l}$  and  $\mathbf{q}_{i-1/2,r}$ .  $\mathbf{A}^- \Delta \mathbf{q}_{i+1/2}$  denotes the fluctuations propagating into the cell at the right face  $x_{i+1/2}$ , with the initial states of the Riemann problem  $\mathbf{q}_{i+1/2,l}$  and  $\mathbf{q}_{i+1/2,r}$ .  $\mathbf{A} \Delta \mathbf{q}_i$  is the total fluctuations inside the cell with  $\mathbf{q}_{i-1/2,r}$  and  $\mathbf{q}_{i+1/2,l}$  as initial states of the Riemann problem.<sup>37,58</sup>

The conservative variables  $\mathbf{q}_{i\pm 1/2,r}$  and  $\mathbf{q}_{i\pm 1/2,l}$  at the cell boundaries are reconstructed by WENO scheme.<sup>53</sup> As the WENO scheme itself is not positivity-preserving, to remedy this problem, the positivity-preserving limiter<sup>50</sup> is used.

Finally, third-order Runge–Kutta scheme is adopted to update the solution

$$\begin{cases} \mathbf{q}^{(1)} = \mathbf{q}^n + \Delta t L(\mathbf{q}^n), \\ \mathbf{q}^{(2)} = \frac{3}{4} \mathbf{q}^n + \frac{1}{4} \mathbf{q}^{(1)} + \frac{1}{4} \Delta t L(\mathbf{q}^{(1)}), \\ \mathbf{q}^{n+1} = \frac{1}{3} \mathbf{q}^n + \frac{2}{3} \mathbf{q}^{(2)} + \frac{2}{3} \Delta t L(\mathbf{q}^{(2)}), \end{cases} \quad (19)$$

where the superscript  $n$  denotes the  $n^{\text{th}}$  time step,  $\mathbf{q}^{(1)}$  and  $\mathbf{q}^{(2)}$  are the intermediate time values.

For 1D computational domain, the nonreflecting boundary conditions applied in the present work are  $d\mathbf{q}/dx|_{\Gamma} = 0$ , where  $\Gamma$  stands for the boundary. The reflective boundary conditions are the same as the nonreflecting boundary conditions except for velocity component perpendicular  $\Gamma$ . For instance, the reflecting boundary condition of velocity component in  $x$ - direction is given as  $u|_{\Gamma} = 0$ .

### C. Adaptive mesh refinement

To improve the computational efficiency, the block-structured AMR method proposed by Berger and Olinger<sup>61</sup> is adopted. This approach makes use of non-overlapped blocks to cover the computational domain, and all blocks are indexed by tree data structure (quad-tree for 2D or oct-tree for 3D). Each block is discretized with identical topology and filled by uniform mesh with buffer layers. As a result, the block-structured AMR method is suitable for implementation of high-resolution schemes with wide stencils.

To gain more insight into the block-structured adaptive mesh, the logical relationships of block, guard cell, and computational cell are depicted in Fig. 1. It is shown that the computational domain is discretized by a series of blocks, and the refinement is performed near the bubble interface [Fig. 1(a)]. Block with buffer layer [Fig. 1(b)] is the basic unit for computation and performing the loading balance algorithm.<sup>62,63</sup> Each block is divided by  $N^3$  uniform mesh ( $N$  is the cell number in one axial direction) and a collocated configuration of physical variables is used as shown in Fig. 1(c).

For the present fifth WENO scheme, four layers of guard cells are introduced as buffer layer for the flux computation at block boundary. On the other hand, the guard cells in the buffer layer can also be used to construct boundary conditions. Therefore, the guard cells should be updated at the end of each time step or after parallel data transmission. When two adjacent blocks are refined by different refinement levels, the fluxes on the block boundaries may not consistent. Additional operations should be performed to ensure the flux conservation. For the guard cells adjacent to refined neighbor blocks, arithmetic average can be used for computing the fluxes. While for the

guard cells adjacent to coarse neighbors, a conservative interpolation approach<sup>33</sup> should be employed.

Refinement criterion used to mark the region to be refined/coarsened is crucial for AMR method. In the present work, a scalar function  $\delta$  is defined as

$$\delta = \sqrt{\left(\frac{\vartheta_{i+1} - \vartheta_{i-1}}{2\Delta x}\right)^2 + \left(\frac{\vartheta_{j+1} - \vartheta_{j-1}}{2\Delta y}\right)^2 + \left(\frac{\vartheta_{k+1} - \vartheta_{k-1}}{2\Delta z}\right)^2},$$

where  $\vartheta$  can be an arbitrary physical field (density, pressure, etc.) of our interest. Two threshold values  $\delta_{min}$  and  $\delta_{max}$  are set to determine which block to be refined or coarsened. To reach the desired accuracy, a preliminary numerical assessment for  $\delta_{min}$ ,  $\delta_{max}$  is necessary. We use the following criterions for refine or coarsen of a block: (1). When  $\delta \geq \delta_{max}$  is detected in one cells of the block, then refine the mesh; (2). when  $\delta \leq \delta_{min}$  is satisfied for any cells of the child blocks, then coarsen to reduce the mesh resolution. In practical, we need to perform preliminary numerical tests to determine  $\delta_{min}$ ,  $\delta_{max}$  until the desired regions are covered with finest mesh. The grid convergence and the comparison with theoretical or experimental results are also helpful to assess the refinement level. In the present work, the phase interface regions should be refined, thus  $\vartheta = \alpha$  with  $\delta_{min} = 0.1$  and  $\delta_{max} = 0.2$  is suggested. The strong discontinuities like shock waves and contact waves are expected to be captured; therefore,  $\vartheta = \rho$  with  $\delta_{min} = 2000$  and  $\delta_{max} = 4000$  is applied.

### III. NUMERICAL VALIDATION FOR 3D BUBBLE COLLAPSE IN OPEN DOMAIN

In this section, the physical process of single bubble collapse in open space is simulated by present AMR solver. The numerical results are compared with theoretical predictions of K–M model. To assess the boundary effects, three sets of the domain size are considered. Mesh independency study are also conducted to test the spatial convergence property of this scheme.

#### A. Numerical tests for the adaptive refinement method and its efficacy

First, the collapse of a single bubble in infinite liquid is considered to test the robustness and efficiency of the AMR solver. The numerical test case shows that the amount of grids in the computational domain will greatly decrease as the bubble compressed. The long period of time simulation, including the re-expansion and re-collapse stage of the collapse process, proves that the present solver is of high robustness.

The computational domain is  $x, y, z \in [0, L]$  with  $L = 20R_0$ , where  $R_0$  is the initial bubble radius. Initially, the bubble is placed at the center of the domain with  $R_0 = 0.038$ . The pressure ratio is  $p_{inf}/p_0 = 100$ , and the initial density ratio  $\rho_{inf}/\rho_0 = 1000$ , where the subscript *inf* denotes the initial pressure in ambient liquid and the subscript 0 denotes the initial pressure inside the bubble. The non-reflecting boundary conditions are applied on all boundaries. The refinement levels 2–9 are adopted, with minimal grid interval  $\Delta x_{min} = R_0/102.4$ . The coarsest refinement level 2 corresponds to the entire domain discretized by  $16 \times 16 \times 16$ , and the finest refinement level 10 corresponds to  $4096 \times 4096 \times 4096$  uniform meshes. The detailed numerical setup could be found in Table I.

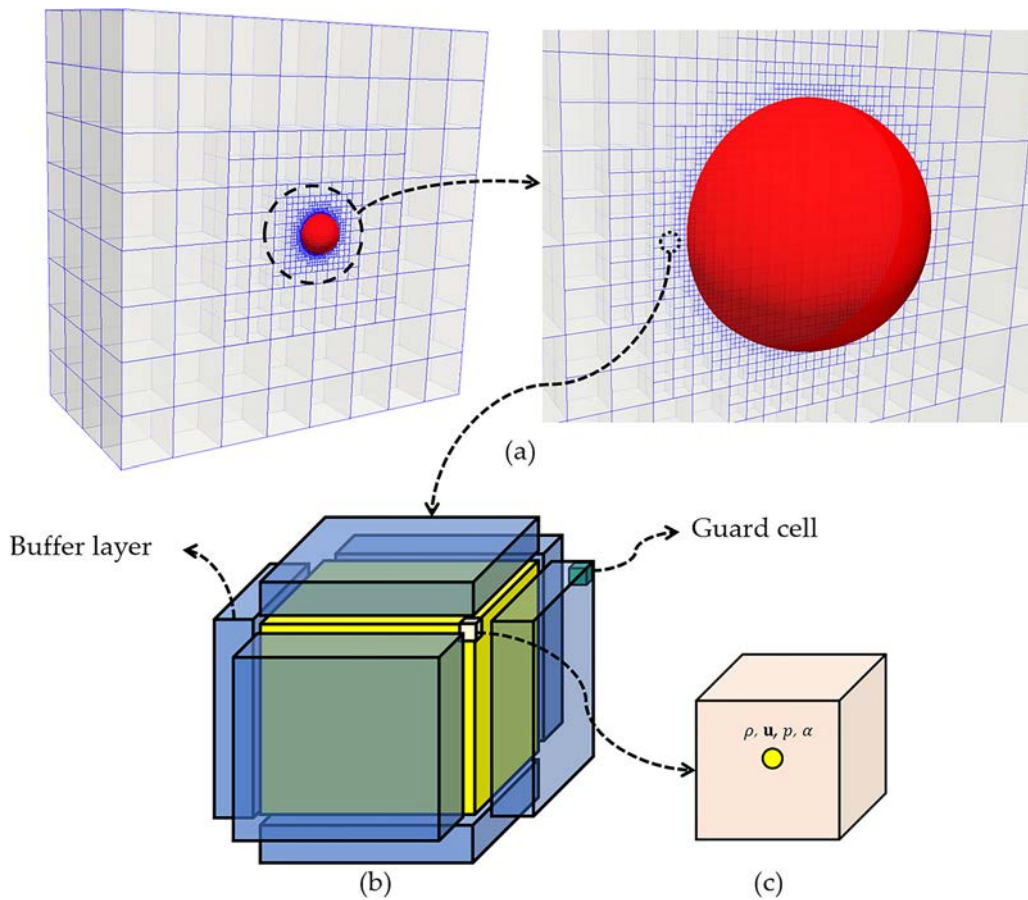


**FIG. 1.** Refinement principle of the block-structured AMR method. (a) Enlarged view of computational domain discretized by a series of blocks for bubble collapse simulation (red surface denotes air bubble), (b) single block that is divided by  $N^3$  uniform mesh with buffer layers outside, and (c) single computational cell in the block with physical variables defined in cell center.

For comparison, the simulation time is scaled by Rayleigh collapse time  $T_c$

$$T_c = 0.915R_0 \sqrt{\frac{\rho_{inf}}{(p_{inf} - p_0)}}$$

**TABLE I.** Parameters of the collapse of a single bubble in infinite liquid. Note that  $|u_i|_{max}$  refers to the maximum velocity in the flow field.

Computational domain size $L_x \times L_y \times L_z$	$20R_0 \times 20R_0 \times 20R_0$
Initial bubble radius $R_0$	0.038
Initial pressure ratio $p_{inf}/p_0$	100
Initial density ratio $\rho_{inf}/\rho_0$	1000
Time step size $\Delta t$	$CFL \times \Delta x_{min}/( u_i _{max} + c)$
CFL (Courant–Friedrichs–Lewy) number	0.3
$\gamma_1$ (liquid)	4.4
$\gamma_2$ (air)	1.4
$p_{\infty,1}$ (liquid)	$6 \times 10^8$
$p_{\infty,2}$ (air)	0.0

Figure 2 shows the evolution of the block at different time instants. As the bubble shrinks, the refined blocks decrease significantly until the bubble volume reaches minimum at about  $1.05T_c$ ; afterward, the blocks count increases as the bubble rebounds. The finest mesh blocks always cover the bubble interface; thus, AMR is crucial to reduce the dissipation of WENO scheme and to maintain the sharpness of the interface. The variation of total block number ( $N_{total}$ ) as a function of time for the entire computational domain is given in Fig. 3.

Figure 4 shows the time history of dimensionless averaged bubble-radius  $R/R_0$  and non-dimensional averaged bubble pressure  $p/p_{inf}$ , where  $R/R_0$  is computed by  $(V/V_0)^{1/3}$ , and  $V$  is calculated from

$$V = \sum_{\Omega} (\Delta x \Delta y \Delta z)_i \times \alpha_i,$$

and  $p$  is derived by

$$p = \frac{1}{V} \sum_{\Omega} (\Delta x \Delta y \Delta z)_i \times \alpha_i \times p_i,$$

where  $(\Delta x \Delta y \Delta z)_i$ ,  $\alpha_i$ , and  $p_i$  denote the volume, gas volume fraction, and pressure of the  $i^{th}$  cell, respectively, and  $\Omega$  represents the whole

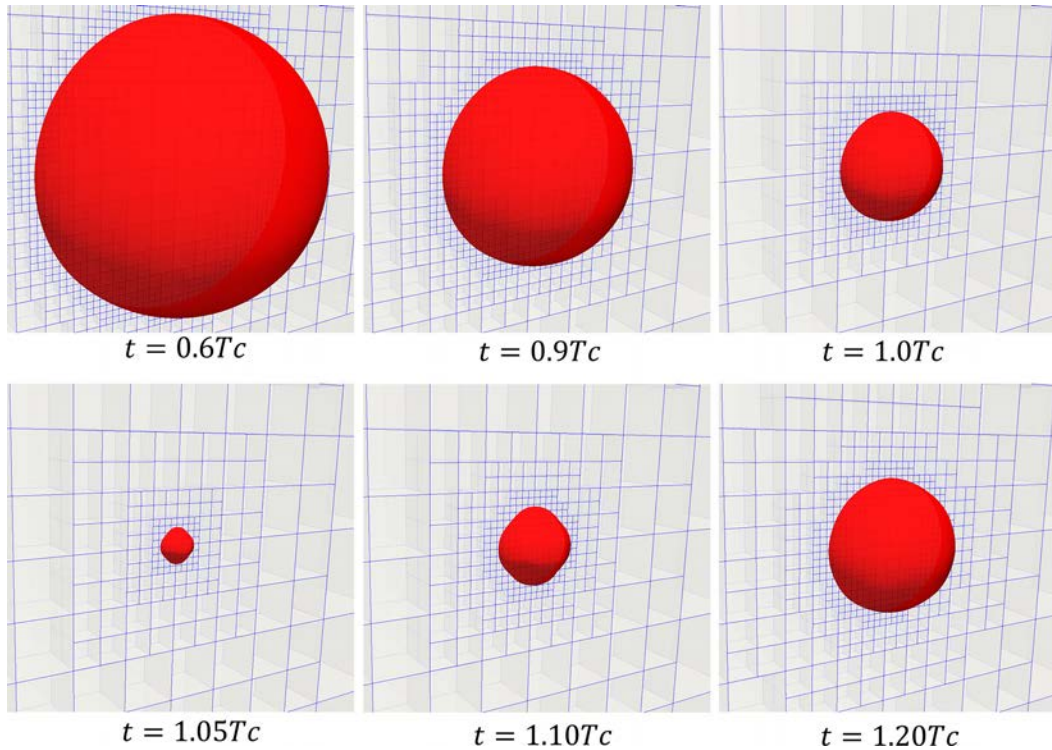


FIG. 2. Block of half computing domain during bubble collapse; each block is discretized by  $N_x = N_y = N_z = 8$ , and the red surface denotes iso-surface of  $\alpha = 0.5$ .

computational domain. We can see the time history of bubble radius and pressure agree well with the K–M solutions, even in the re-collapse and re-expansion stage; thus, it can be concluded that the present developed AMR solver is capable in simulating the dynamic behaviors of an oscillating bubble.

**B. Computational domain and mesh independency study**

The convergence study of computational domain is conducted to assess the boundary effects. Three cubic computational domains of  $x, y, z \in [0, L]$  with  $L = 10R_0, 20R_0,$  and  $40R_0$  are considered. The

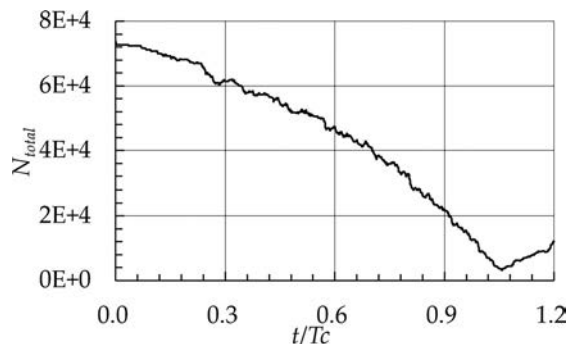


FIG. 3. Blocks count ( $N_{total}$ ) during the simulation of single bubble collapse in open space.

same initial and boundary condition setups are used as in Sec. III A. For the three domain sizes, the corresponding refinement levels are set as 2–8, 2–9, and 2–10 to keep the finest mesh resolutions consistent, thus  $R_0/\Delta x_{min} = 102.4$  is maintained for all of the three cases. Figure 5 displays the numerical results with different domain size. It is found that time evolution of bubble radius and pressure converge with the increase in domain size, even with  $L = 10R_0$ , only slight discrepancies near the peak values are shown. In order to minimize the effects of the far-field boundaries,  $L = 20R_0$  is considered in the following simulations.

Next, the grid convergence study on adaptive mesh is performed. The refinement levels of 2–6, 2–7, 2–8, and 2–9 are tested with the same size computational domain  $L = 20R_0$ , and the finest refinement level 6, 7, 8, and 9 correspond to  $R_0/\Delta x_{min} = 12.8, 25.6, 51.2,$  and  $102.4$ , respectively. As shown in Fig. 6, both  $R/R_0$  and  $p/p_{inf}$  show good convergence properties; except for the refinement levels of 2–6, slight discrepancies near the peak values are shown. To reduce the computing expense and keep high accuracy, the refinement level 2–9 is adopted in the following work.

**C. Comparison with theoretical predictions**

To further validate and assess the reliability of the present AMR solver, single bubble collapse in open space with different driven pressures and initial bubble radii are considered, and the numerical results are compared with K–M solutions.<sup>20</sup> Figure 7 presents the results of the bubble collapse with the initial radius  $R_0 = 0.038$  under three driven pressures,  $\frac{p_{inf}}{p_0} = 10, 20,$  and  $100$ . For higher pressure-ratio cases, bubble will be compressed into much smaller size with violent

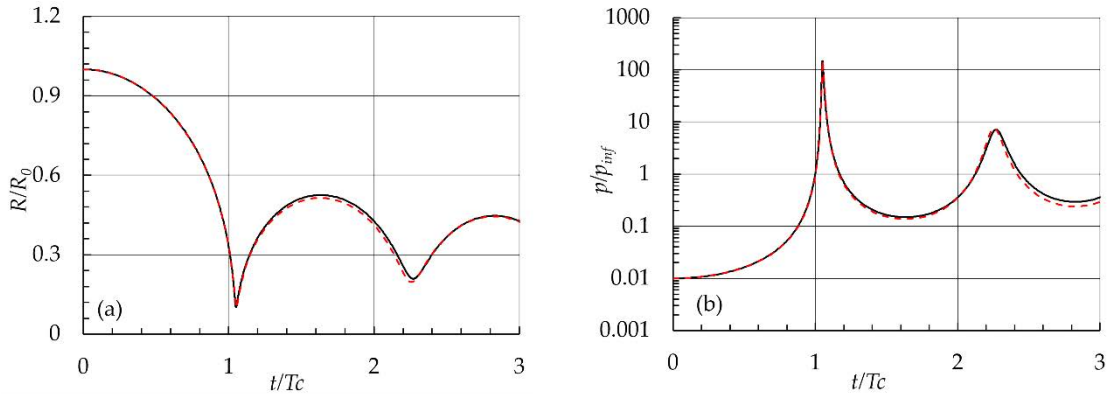


**FIG. 4.** Comparison of present numerical results (red dashed line) and the K–M solutions (black line) for single bubble collapse with the initial radius  $R_0 = 0.038$ , and the driven pressure is  $p_{inf}/p_0 = 100$ : (a) averaged bubble radius and (b) averaged pressure.

rebounding. Figure 7 illustrates that, even for  $p_{inf}/p_0 = 100$ , the time history of  $R/R_0$  and  $p/p_{inf}$  agrees well with the theoretical solutions from the K–M equation; both the peak values and collapse durations are predicted accurately.

Bubble collapse with smaller initial radius  $R_0 = 0.01$  and  $R_0 = 0.001$  under the same driven pressure  $p_{inf}/p_0 = 100$  is also simulated for comparison. Even for the smaller bubble size, the time history of the averaged bubble radius shows good agreements with theoretical solutions, and the peak values of the average pressure inside the bubble are also predicted accurately as displayed in Fig. 8.

From Figs. 7 and 8, it can be observed that even considering different cases of driven pressures and initial radii, all cases show similar final collapse instant (around  $1.05Tc$ ). Generally, the bubble compressing and the first rebounding process are predicted accurately, so the accuracy of present numerical approaches is further proved.

#### IV. HIGH-FIDELITY SIMULATION OF BUBBLE COLLAPSE NEAR SOLID WALL

##### A. Evolution of wall pressure in the bubble collapse near a solid wall

In this section, the wall pressure, shock wave, and re-entrant jet in the collapse of a 3D bubble near a planar solid wall are investigated.

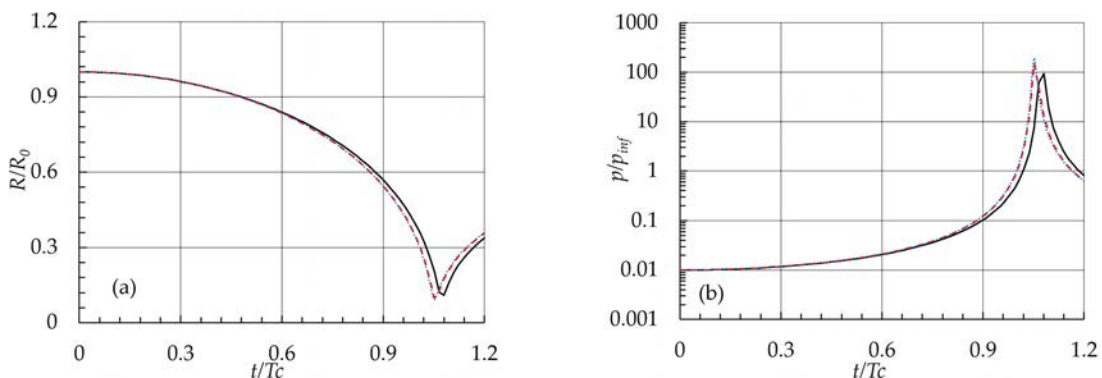


**FIG. 5.** Convergence study of the domain size for the simulation of single bubble collapse in liquid: the driven pressure is  $p_{inf}/p_0 = 100$ , and time history of (a) averaged bubble radius and (b) averaged pressure inside bubble is shown. Black line:  $L = 10R_0$  with refinement level 2–8; red dashed line:  $L = 20R_0$  with refinement level 2–9; blue dotted line:  $L = 40R_0$  with refinement level 2–10.

Geometry of computational domain is  $x, y, z \in [0, L]$  as shown in Fig. 9, where  $L = 20R_0$ . The reflective boundary conditions are applied on the solid wall, and the nonreflecting boundary conditions are considered on the other boundaries. Since the collapse of a single bubble can be regarded as a symmetric problem, one-quarter of the computational domain is adopted by applying symmetry boundary conditions along the relevant cross sections. In Fig. 9 and the following analysis, the proximal side always denotes the leftmost side of the bubble near the solid wall, and the distal side indicates the rightmost side of the bubble.

The initial bubble radius is  $R_0 = 0.62$ , and the initial stand-off distance from the bubble center to the solid wall is  $H_0 = 1.5R_0$  in the following work, unless stated otherwise. The detailed initial parameters of liquid and gas are given by

$$[\rho_1 \alpha_1, \rho_2 \alpha_2, u, p, \gamma, p_\infty, \alpha] = \begin{cases} [0, 1, 0, 1.06, 1.4, 0, 1], & 0 \leq r < R_0, \\ [1000, 0, 0, 374, 6.59, 4049, 0], & R_0 \leq r, \end{cases} \quad (20)$$

and all the parameters above are dimensionless values.

Figure 10 shows the variation of bubble shape, with the pressure contour on the solid wall and velocity field on the cross section of  $z = 0.5L$ . Initially, the bubble collapses non-spherically toward the

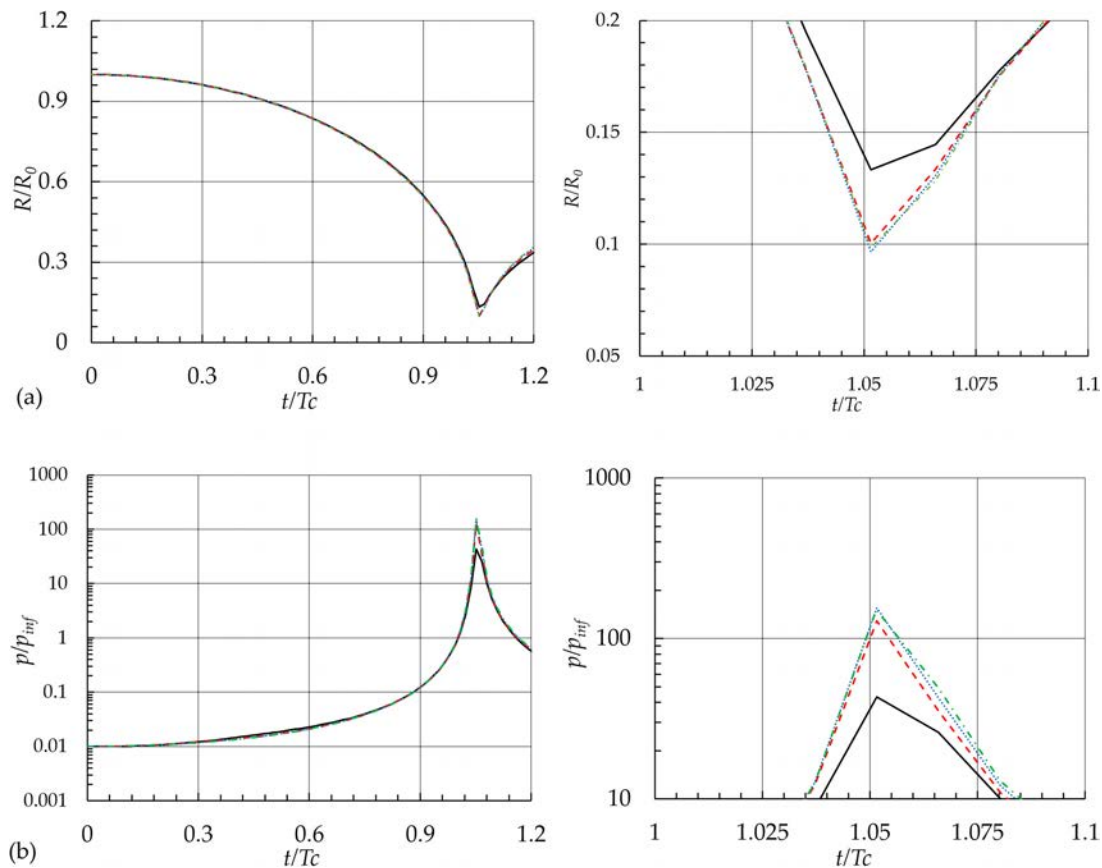


**FIG. 6.** Mesh independency study for simulating single bubble collapse in liquid: the driven pressure is  $p_{inf}/p_0 = 100$ , and time history of (a) averaged bubble radius and (b) averaged pressure inside bubble (with an enlarge view in the right) is shown. Black line:  $L = 20R_0$  with refinement level 2–6; red dashed line:  $L = 20R_0$  with refinement level 2–7; blue dotted line:  $L = 20R_0$  with refinement level 2–8; green dashed-dotted line:  $L = 20R_0$  with refinement level 2–9.

planar wall driven by pressure difference. The distal side of the bubble first contracts, then involutes, and finally forms a re-entrant jet; this physical process is similar to the pioneering work of Plesset and Chapman.<sup>25</sup> After the re-entrant jet penetrates the proximal side of bubble, the bubble splits into several toroidal bubbles by the catapulting jet, and these toroidal bubbles move toward the solid wall with violent deformations and impinge on the solid wall in the end. According to the evolution of pressure distribution on the solid wall surface in Fig. 10, the high pressure appears on the center of the wall and gradually reaches maximum until  $1.27T_c$ ; shortly after, the high pressure on the wall surface evolves into a circle region and propagates outward radially, while at the same time, the pressure on the wall center decreases until the re-entrant jet collides with the wall surface. When the pressure on the wall center reaches up to the maximum value, the re-entrant jet does not contact with the wall surface and the velocity contours on the cross section  $z = 0.5L$  also show that the high speed flow not yet contact with the wall surface. As a result, it can be inferred that the maximum pressure on the wall does not result from the jet impacting.

Figure 11 displays the time history of the pressure on the wall center and averaged bubble radius. In the initial stage of the collapse, the pressure increases very slowly until  $1.22T_c$ ; shortly after, the pressure rapidly reaches up to maximum value (note that the bubble radius

achieves its minimum volume at about  $1.18T_c$ ). At about  $1.27T_c$ , the pressure on the wall center reaches its first peak value, and later, the pressure decreases rapidly to its minimum at about  $1.37T_c$ ; shortly after, the pressure increases to the secondary peak; however, the pressure magnitude is smaller than the first peak. At this instant ( $1.37T_c$ ), the tip of the re-entrant jet impacts the solid wall. After that, the pressure on the wall center experiences a gradual decrease.

Pressure peaks acting on the wall center play an important role of cavitation erosion; thus, it is of great importance to identify the reasons for the first pressure peak appearing in Fig. 11. To this end, the shock waves induced initially in the collapse process are studied. According to the evolution of pressure gradients field (Fig. 12), the shock wave emitted by the collapsed bubble propagates toward the wall and finally results in high pressure on the wall center. Therefore, the shock wave emission in the collapse process is proven to be the primary reason for the first peak pressure on the solid wall and the re-entrant jet impacting on the solid wall accounts for the second peak pressure. However, there are a few experimental and numerical researches focusing on shock wave emission process of a collapsing bubble, and the mechanisms of shock wave formation and evolution are still unclear. In order to gain more insight into the shock wave emission process, a comprehensive study of the shock waves upon bubble collapse is performed.

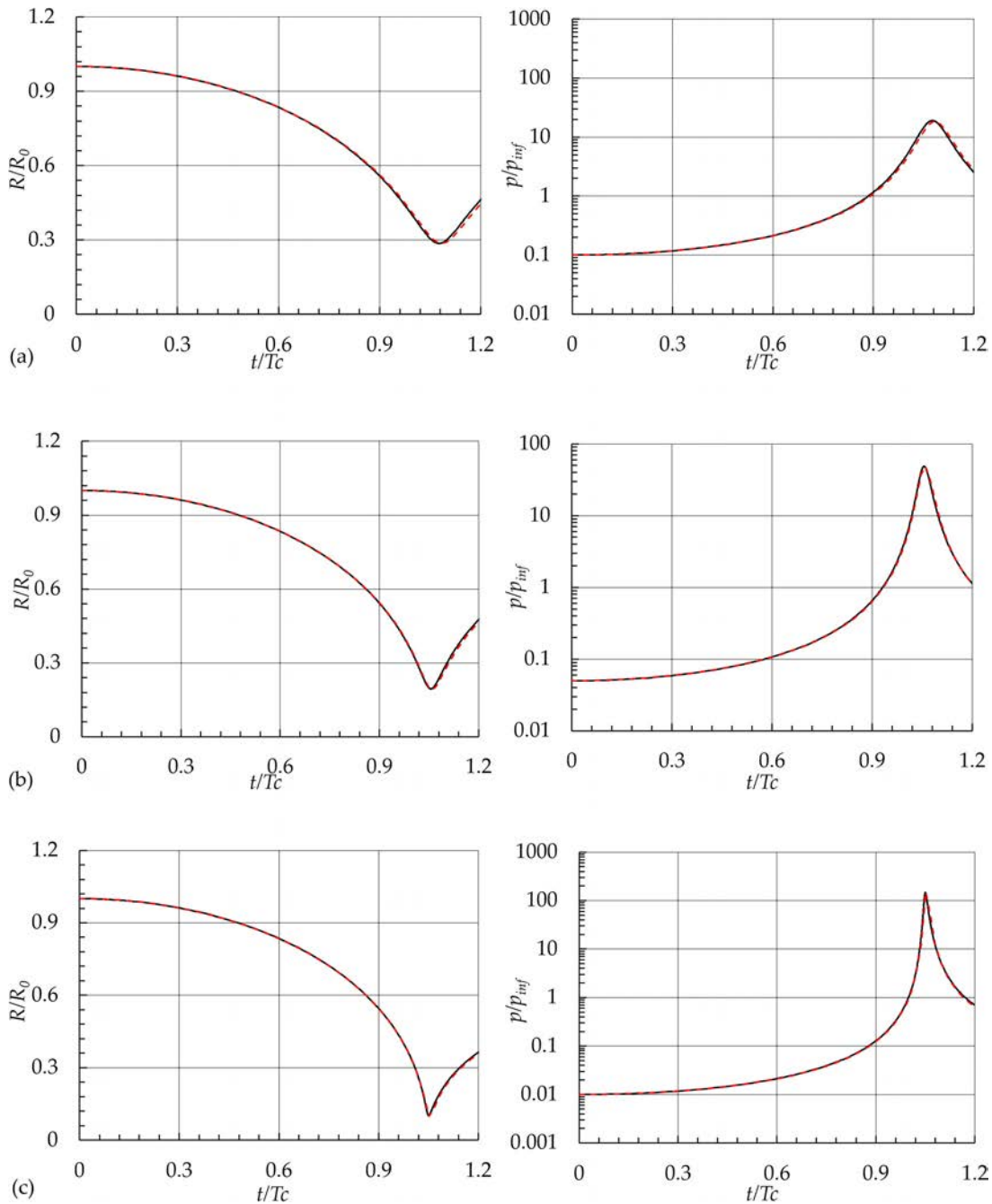


**FIG. 7.** Comparison of present numerical results (red dashed line) and the K–M solutions (black line) of the averaged bubble radius (left) and pressure history (right) for single bubble collapse, with the same initial radius  $R_0 = 0.038$  and (a)  $p_{inf}/p_0 = 10$ , (b)  $p_{inf}/p_0 = 20$ , and (c)  $p_{inf}/p_0 = 100$ .

**B. Formation of shock waves in the collapse process**

The formation of a precursor shock ahead of the water-hammer shock was observed in the experiment by Ohl *et al.*<sup>64</sup> As stated by Lindau and Lauterborn,<sup>65</sup> the water-hammer pressure is partly caused by precursor shock, while Johnsen and Colonius<sup>44</sup> explained that the piston-like

motion of the re-entrant jet leads to the generation of precursor shock. To clarify the generation of water-hammer shock, the entire process of near-wall bubble collapse is simulated by the present AMR solver.

Figure 13 presents the pressure gradient ( $|\nabla p|$ ) field on the cross section  $z = 0.5L$ . When the distal side of bubble deforms inward the

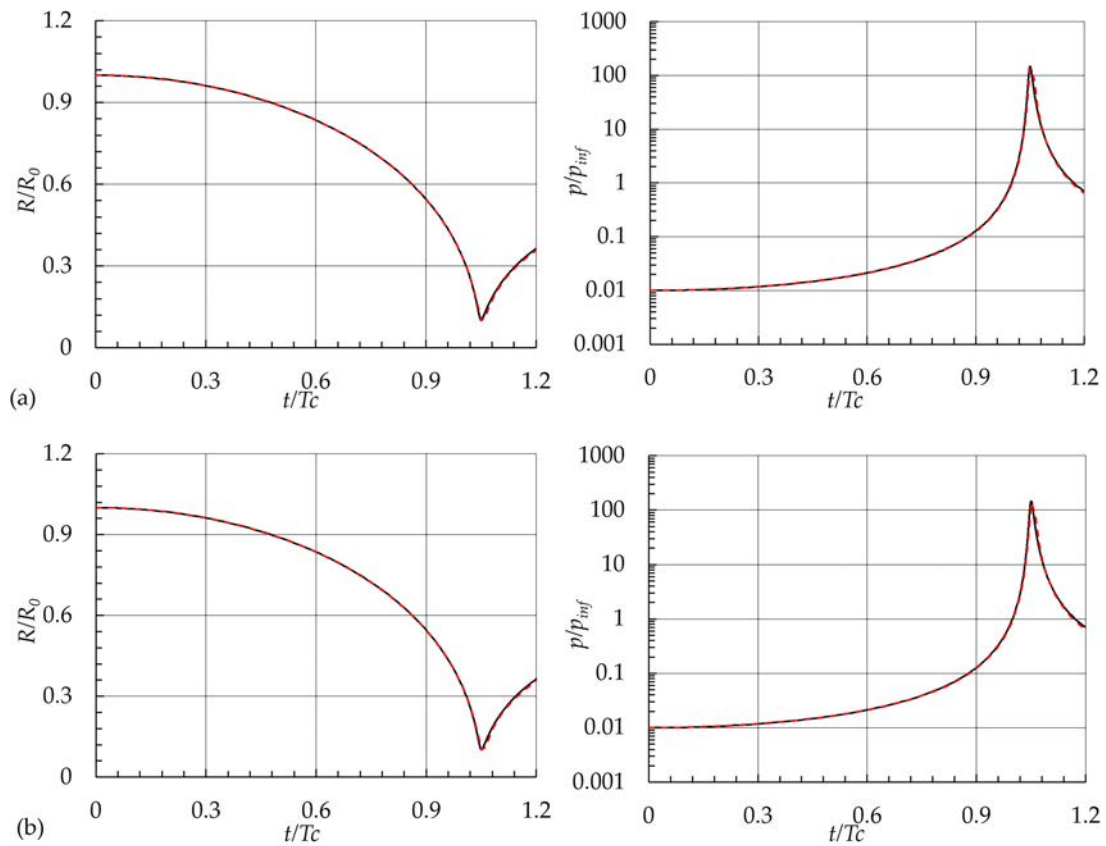


**FIG. 8.** Comparison of the present numerical results (red dashed line) and the K–M solutions (black line) of the averaged bubble radius (left) and pressure history (right) for single bubble collapse; the initial radius of (a)  $R_0 = 0.01$ , (b)  $R_0 = 0.001$  with the same driven pressure  $p_{inf}/p_0 = 100$  is considered.

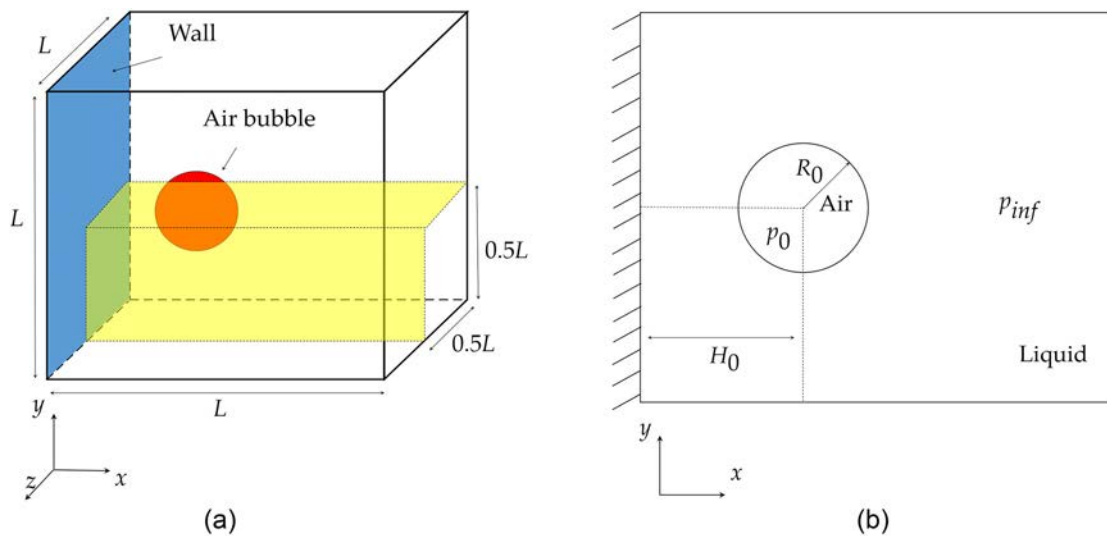


**FIG. 9.** Schematic diagram of computational domain for bubble collapse near solid wall: (a) geometric configuration, the blue surface in the left side of the computational domain is the solid wall and the red sphere denotes the air bubble, the symmetry boundary conditions are applied on the yellow cross sections; (b) cross section of  $z = 0.5L$ .

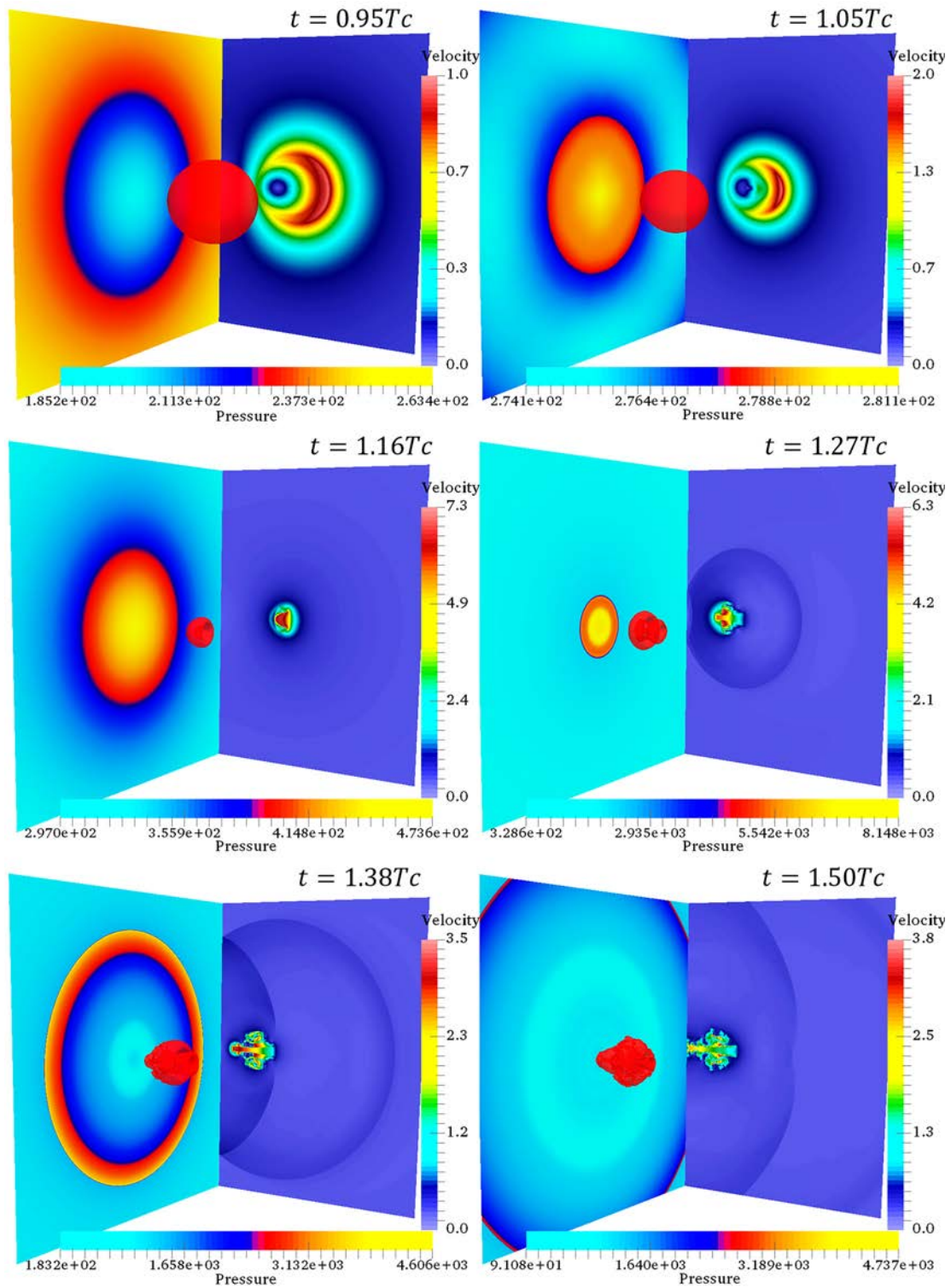


**FIG. 10.** Pressure contours on the wall surface, velocity fields on the cross section  $z = 0.5L$ , and bubble profiles during bubble collapse at different time instants; the red surface denotes iso-surface of  $\alpha = 0.5$ .

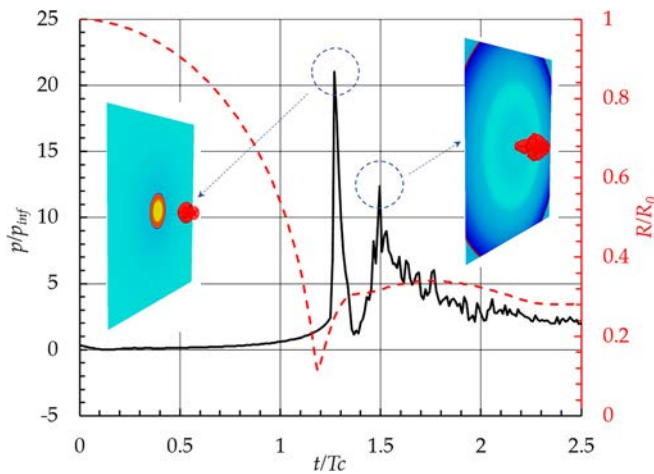


**FIG. 11.** Time history of wall pressure (black line) and averaged bubble radius (red dashed line); two pressure fields corresponding to the instants of the two pressure peaks are presented.

bubble, a shock wave generates inside the bubble; it becomes more visible as the advancing of re-entrant jet. The shock wave propagates toward the proximal side and is refracted at  $1.170Tc$ . Subsequently, a precursor transmitted shock is formed in the liquid, together with a reflected shock inside the bubble ( $1.171Tc$ ). With the precursor shock propagating away from the bubble interface, the reflected shock penetrates the tip of the re-entrant jet into the liquid at  $1.172Tc$ . Shortly after the re-entrant jet impacting on the proximal side of bubble, a more intense water-hammer shock wave is emitted. The water-hammer shock toward the solid wall merges with the precursor shock at  $1.176Tc$ . More shock waves with complex interference are observed on the bubble tip region ( $1.176Tc$ ); two visible shocks propagating inside the toroidal bubble at  $1.176Tc$  and  $1.184Tc$  are also captured. It is noted that the shape of the bubble interface is almost undistorted after the shock inside the bubble penetrates the bubble tip. As the water-hammer shock propagates, finally an approximately spherical shape is developed ( $1.184Tc$ ).

Numerical simulations show that the piston-like re-entrant jet may lead to a rapid compression process of the gas and create shock

wave inside the bubble due to the pressure difference. To clarify the relations between the precursor shock and the re-entrant jet, the evolution of pressure field inside the bubble is analyzed.

### C. Relations of pressure and shock waves

In this section, the shock generation and emission, shock–interface, shock–shock interactions as well as the relations between shocks and pressure field are investigated quantitatively. Figure 14 shows the pressure distribution and pressure gradient on the partial cross section  $z = 0.5L$ . As time elapses, the high-pressure region is found around the distal side of bubble, giving rise to the deformation of bubble interface. As the distal side of bubble developing into a re-entrant jet, the pressure jump inside the bubble becomes visible gradually (Fig. 14). Figure 15 shows the pressure and volume fraction along the centerline of the computational domain at different time instants. At  $1.141Tc$ , the pressure discontinuity inside bubble is formed in front of the re-entrant jet. As the bubble is compressed more, the pressure on the distal side increases rapidly, and a sharp pressure jump is observed at  $t = 1.163Tc$  and  $t = 1.168Tc$ . It is shown that the left pressure peak always appears on the distal side of the bubble as the deforming of the interface [Figs. 15(c) and 15(d)].

Shock wave generated inside the bubble will impact the bubble interface ahead of the re-entrant jet impinging on the proximal side of the bubble, and an abrupt increase in pressure (Fig. 16) in the bubble tip region is observed. Figure 17 depicts the process of shock–interface interaction from the instant when the shock wave inside the bubble penetrates the bubble interface. It can be seen that the pressure on the proximal side of bubble increases rapidly forming a pressure peak, which is much higher than the pressure in the ambient liquid. As shown in Figs. 17(c)–17(f), two pressure discontinuities are generated around the proximal bubble interface, corresponding to the transmitted and reflected shock wave in Fig. 16. After the shock penetrates the bubble interface, the pressure peak on the proximal side of bubble almost reaches up to  $60p_{inf}$  ( $1.170Tc$ ). The transmitted shock wave propagates into the liquid forming a precursor shock, followed by a reflected shock wave propagating inside the bubble as shown in Fig. 16.

Shortly after the shock wave refracting at the proximal side of the bubble, the re-entrant jet contacts with the bubble interface leaving a higher pressure region as displayed in Fig. 18. Subsequently, the bubble splits into a toroidal-shape bubble, followed by the emission of

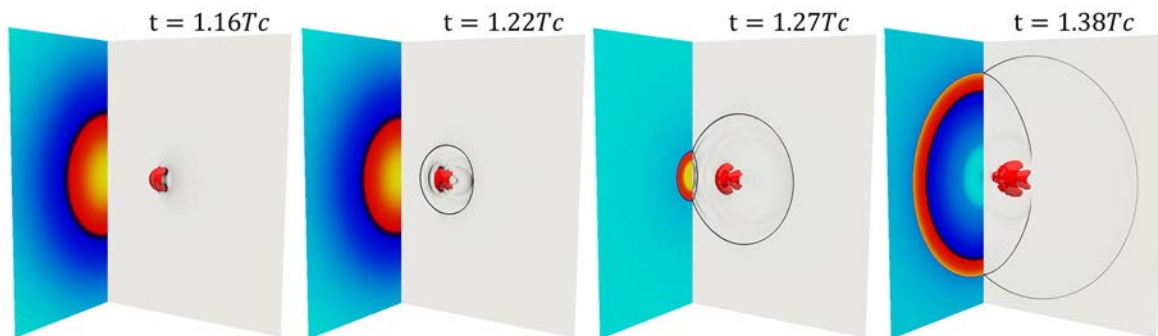


**FIG. 12.** Pressure gradients (right) on cross section  $z = 0.5L$  at different time instants, together with the pressure field on solid wall (left); the red surface denotes iso-surface of  $\alpha = 0.5$ .

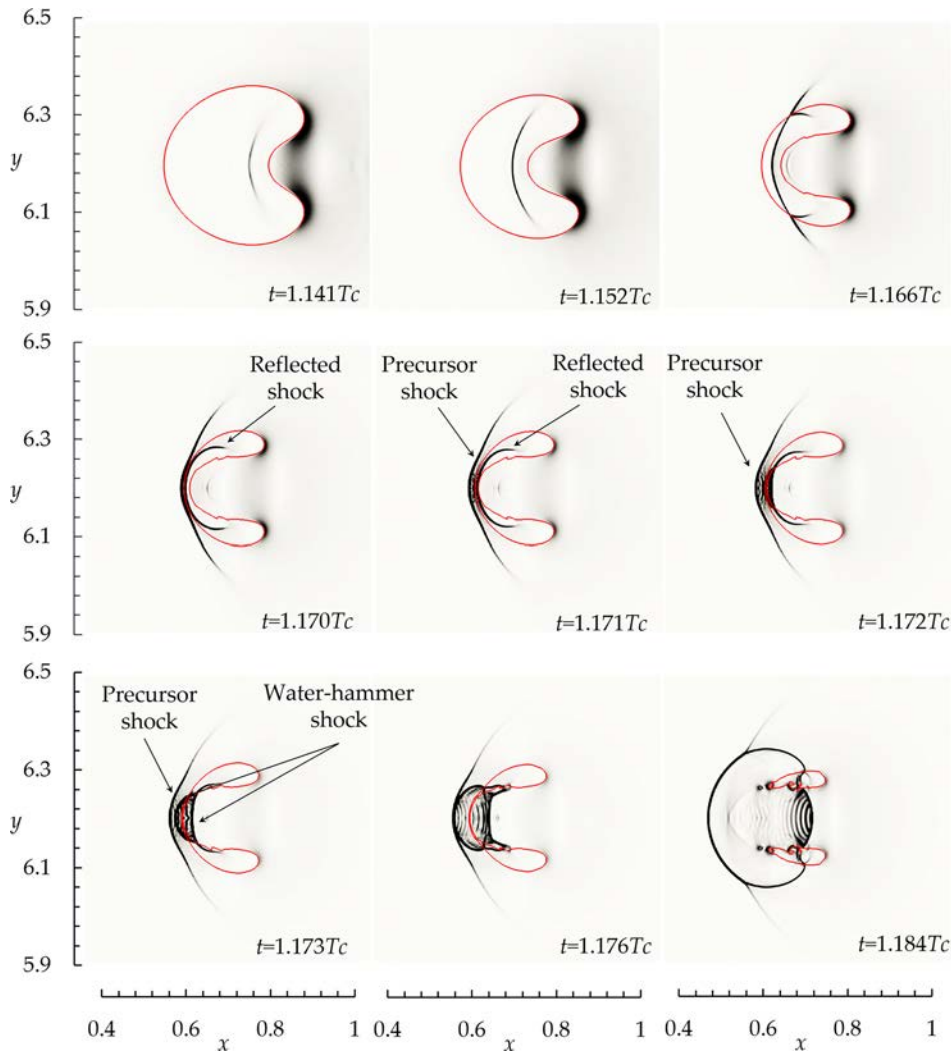


FIG. 13. Pressure gradient contours on the cross section  $z = 0.5L$  at different time instants:  $x = 0$  corresponds to the position of the solid wall, and the red line denotes iso-surface of  $\alpha = 0.5$ .

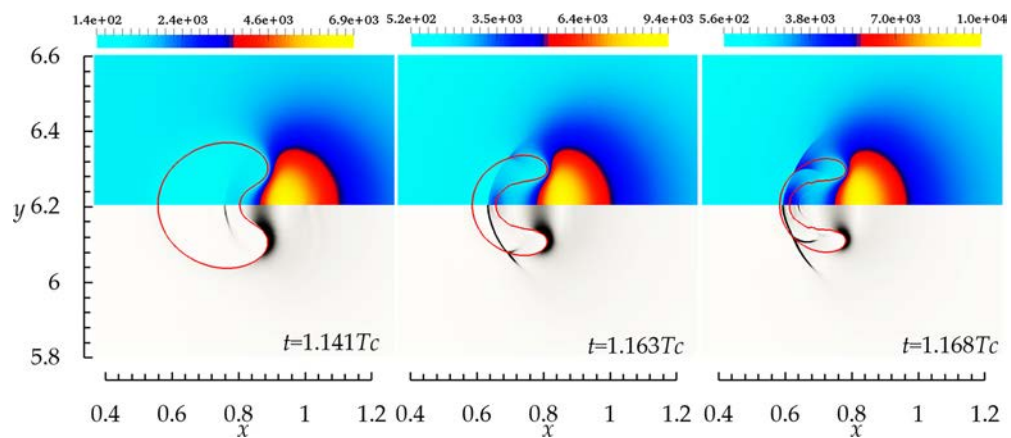
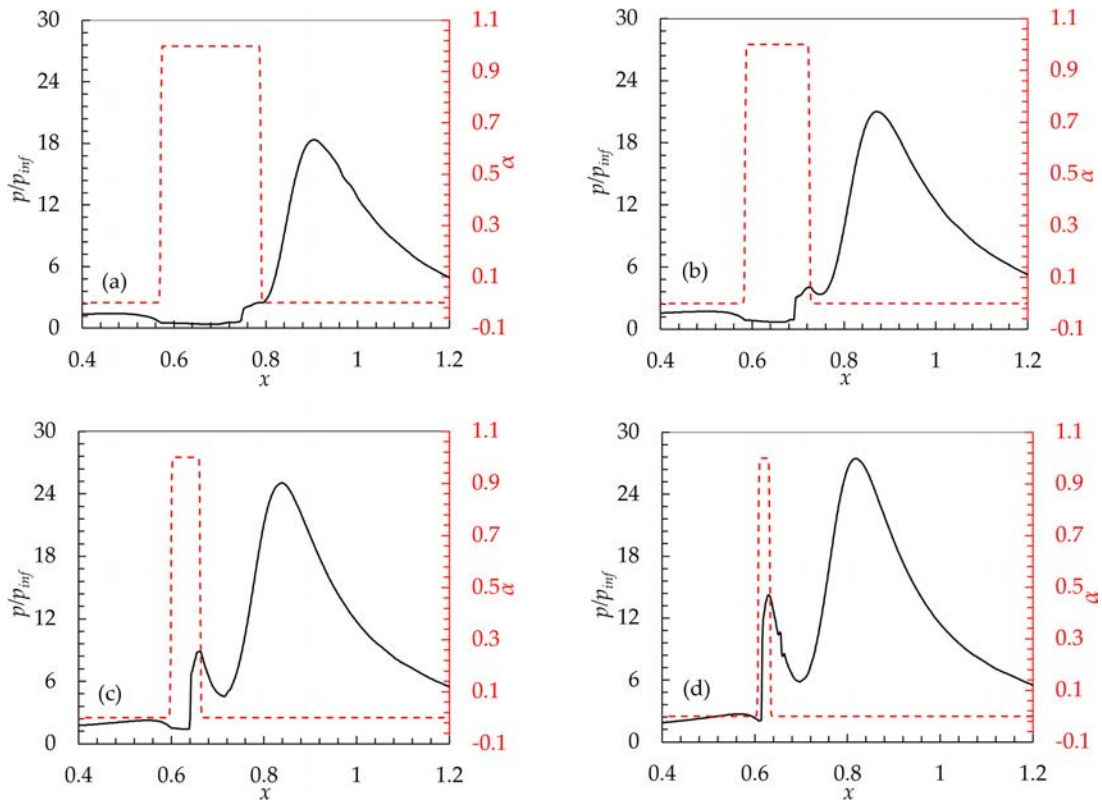


FIG. 14. Pressure (top) and pressure gradient  $|\nabla p|$  (bottom) contours on the cross section  $z = 0.5L$  at different time instants:  $x$  denotes the distance from the solid wall and  $x = 0$  is the location of the solid wall, and the red line denotes iso-surface of  $\alpha = 0.5$ .



**FIG. 15.** Pressure and volume fraction on the centerline from  $x = 0.4$  to  $x = 1.2$ , at instants (a)  $t = 1.141T_c$ , (b)  $t = 1.152T_c$ , (c)  $t = 1.163T_c$ , and (d)  $t = 1.168T_c$ . Black line: Pressure; red dashed line: volume fraction.

water-hammer shock. The water-hammer shock propagates in liquid radially and merges with the precursor shock at about  $1.1743T_c$ . In Fig. 19, it can be found that the reflected shock impacts the tip of the re-entrant jet and generates a much higher pressure peak (up to  $135p_{inf}$ ) in liquid phase. It is noted that the high-pressure region

spreads in the entire domain, including regions away from the wall (Fig. 18). When the re-entrant jet impacts the proximal side of bubble [Fig. 19(e),  $1.1722T_c$ ], another peak pressure appears at the contact region, such that the water-hammer shock is generated ( $1.1728T_c$ ) accordingly. Figure 19(g) shows that the water-hammer pressure

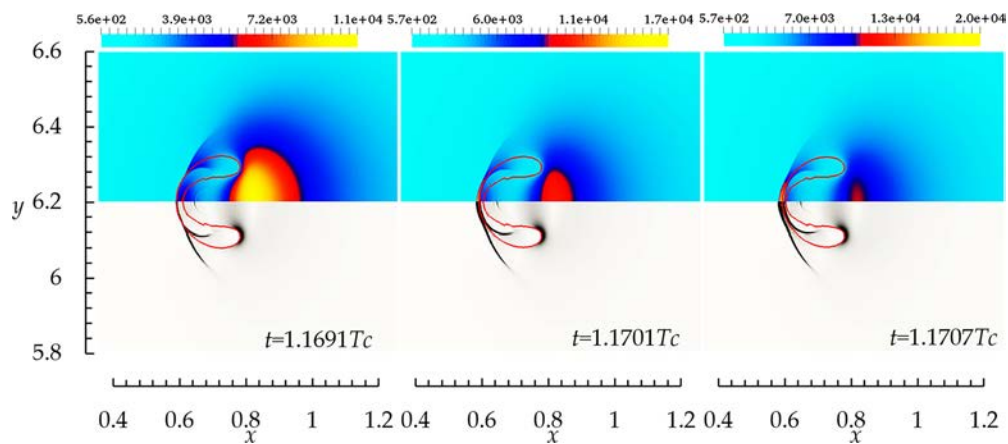


**FIG. 16.** Pressure (top) and pressure gradient (bottom) contours on the cross section  $z = 0.5L$  at different time instants,  $x = 0$  is the location of the solid wall, the red line denotes iso-surface of  $\alpha = 0.5$ .

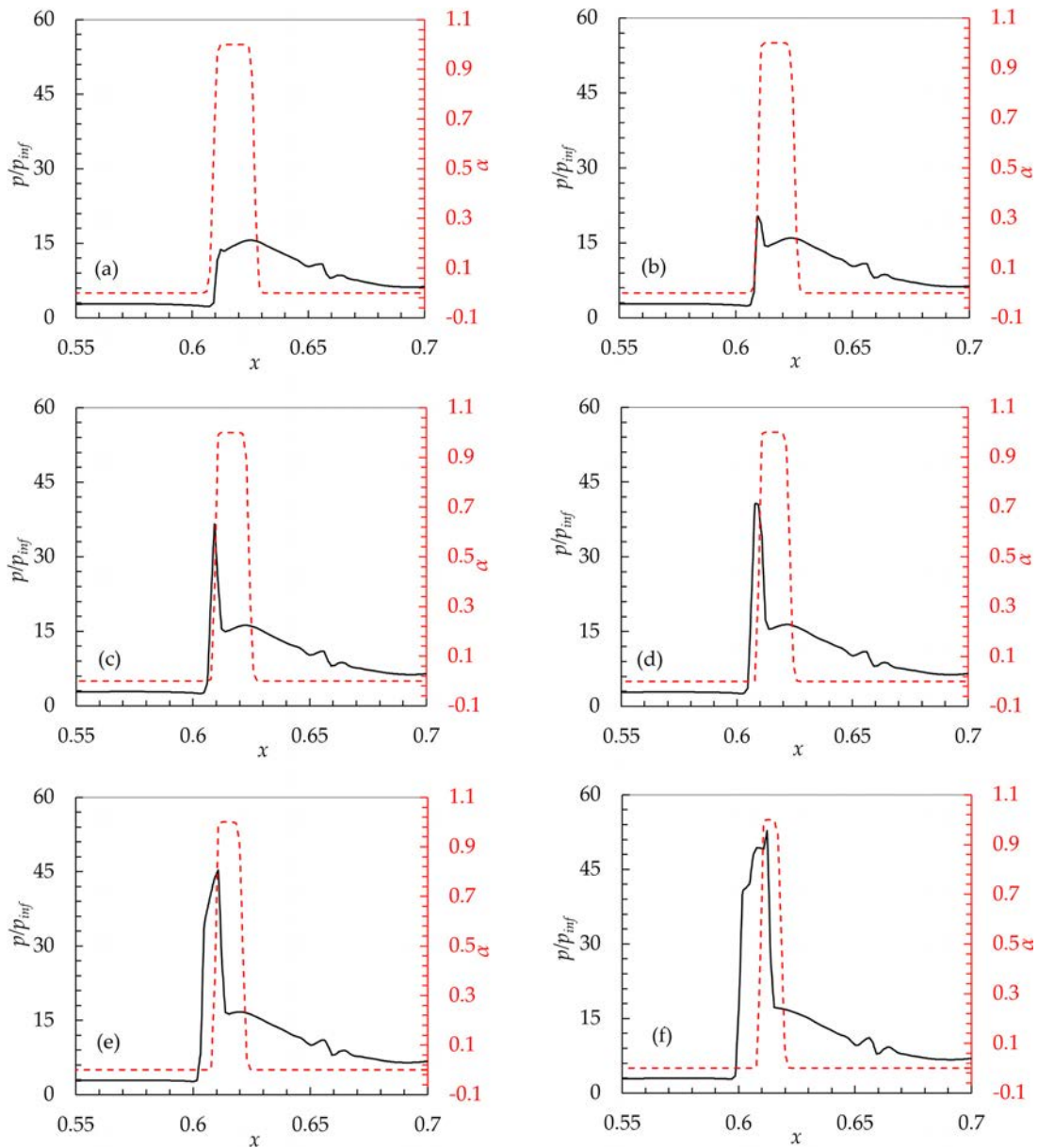


**FIG. 17.** Pressure and volume fraction on the centerline from  $x = 0.55$  to  $x = 0.7$ , at instants (a)  $t = 1.1691T_c$ , (b)  $t = 1.1694T_c$ , (c)  $t = 1.1696T_c$ , (d)  $t = 1.1698T_c$ , (e)  $t = 1.1701T_c$ , and (f)  $t = 1.1707T_c$ . Black line: Pressure; red dashed line: volume fraction.

increases up to maximum at about  $1.1733T_c$ , with the magnitude almost equal to the peak pressure generated by the collision of reflected shock and the re-entrant jet [Fig. 19(c)]. In the final stage, water-hammer shock toward the wall merges with the precursor shock at  $1.1756T_c$ . In Figs. 19(g) and 19(h), the water-hammer shock moving away from the solid wall dissipates gradually and makes the reflected shock sharper, but does not merge with the reflected shock. According to Fig. 19, it can be concluded that the impact of the re-entrant jet on the reflected shock occurs before the generation of the water-hammer shock, which strengthens the reflected shock.

As aforementioned, the precursor shock and water-hammer shock are emitted during the collapse, which may have great potential damage to the planar wall; thus, the evolutions of the pressure field after shock wave emission are also discussed. Figure 20 presents the instantaneous pressure curves after the water-hammer shock and precursor shock are merged. At the beginning, pressure waves with two visible peaks propagate in opposite direction. The left pressure peak is dissipated rapidly while the right pressure shock is strengthened as it propagating away from the wall. A large pressure peak is generated when the top and bottom water-hammer shocks are focused, with

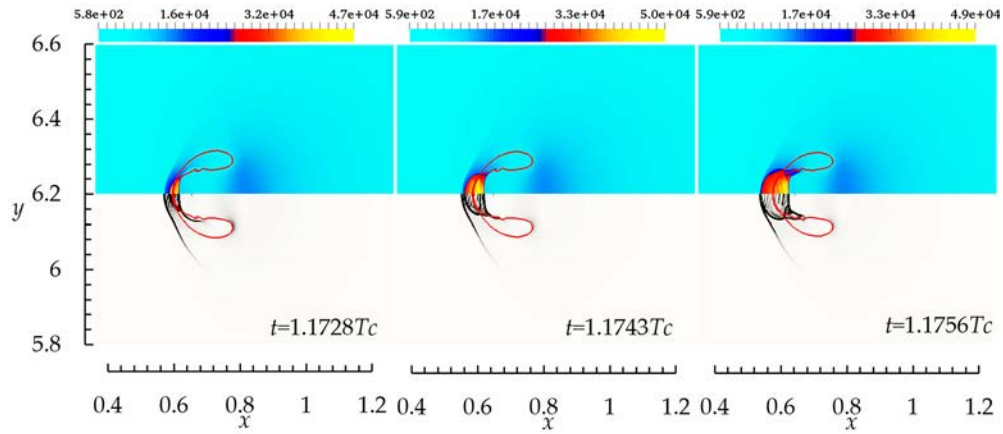


**FIG. 18.** Pressure (top) and pressure gradient (bottom) contours on the cross section  $z = 0.5L$  at different time instants:  $x$  denotes the distance from the solid wall and  $x = 0$  is the location of the solid wall; the red line denotes iso-surface of  $\alpha = 0.5$ .

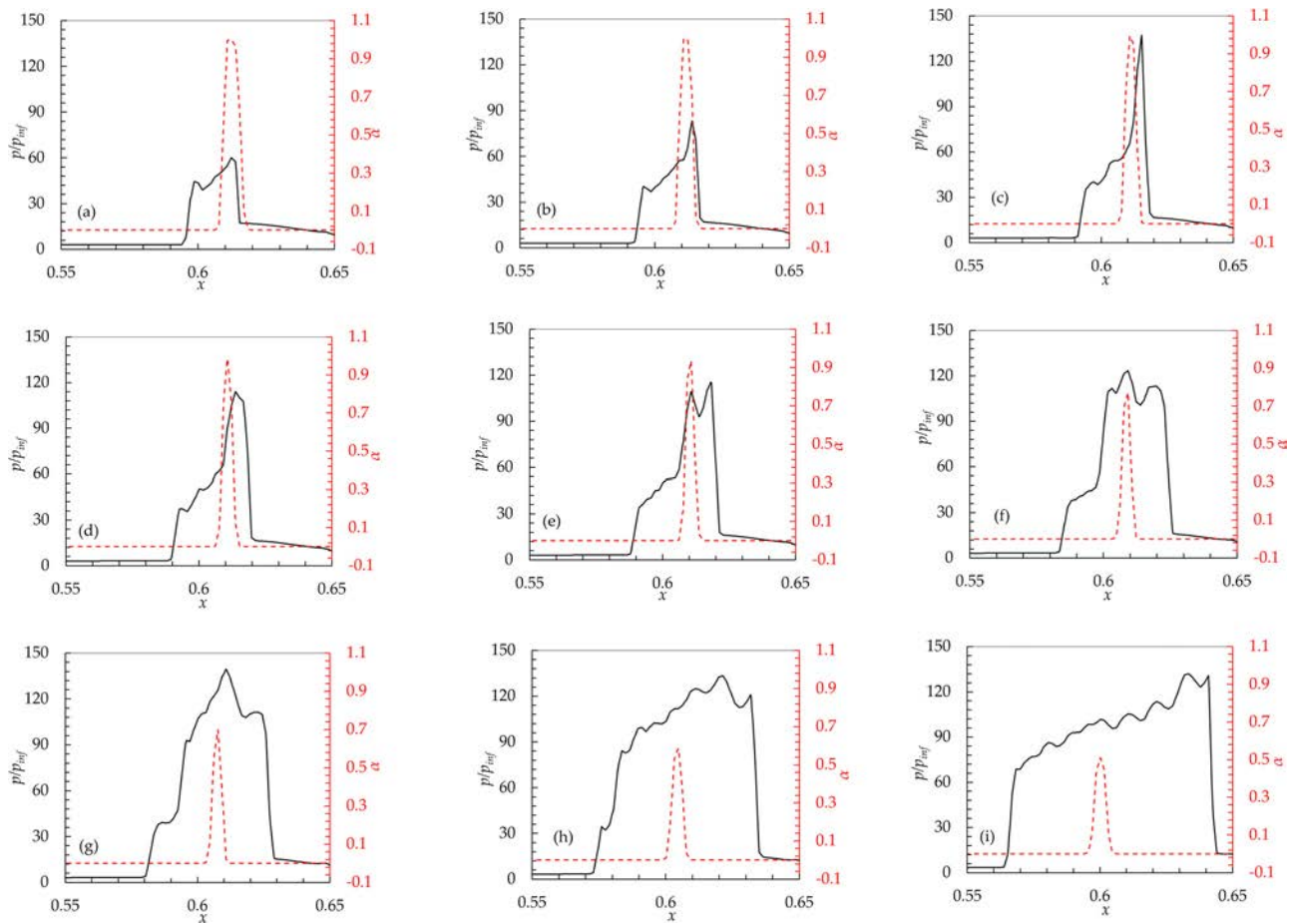


**FIG. 19.** Pressure and volume fraction on the centerline from  $x = 0.55$  to  $x = 0.65$ , at instants (a)  $t = 1.1712T_c$ , (b)  $t = 1.1715T_c$ , (c)  $t = 1.1718T_c$ , (d)  $t = 1.1720T_c$ , (e)  $t = 1.1722T_c$ , (f)  $t = 1.1728T_c$ , (g)  $t = 1.1733T_c$ , (h)  $t = 1.1743T_c$ , and (i)  $t = 1.1756T_c$ . Black line: Pressure; red dashed line: volume fraction.

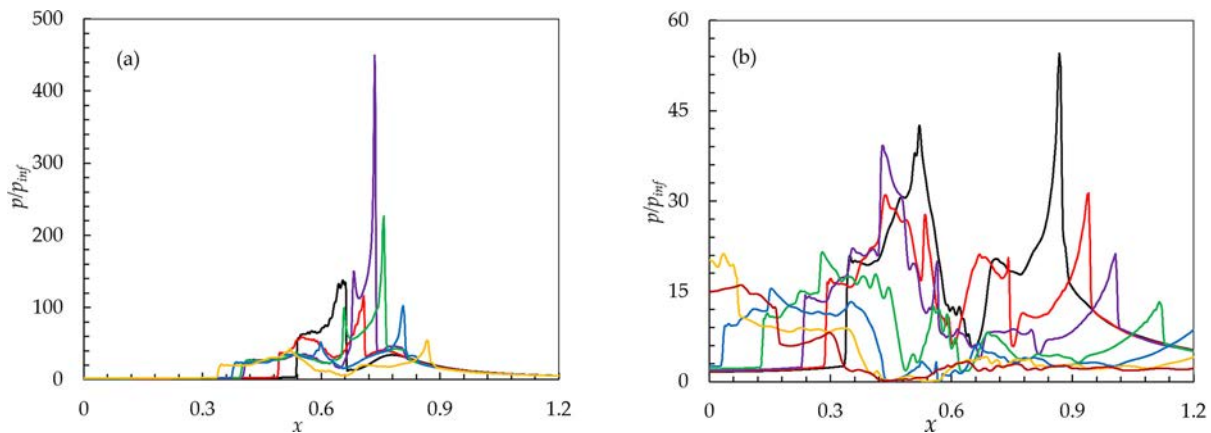


**FIG. 20.** Evolution of pressure distribution on the centerline from  $x = 0$  to  $x = 1.2$ . (a) Black line:  $t = 1.179T_c$ , red line:  $t = 1.184T_c$ , purple line:  $t = 1.196T_c$ , green line:  $t = 1.197T_c$ , blue line:  $t = 1.2T_c$ , yellow line:  $t = 1.206T_c$ ; (b) Black line:  $t = 1.206T_c$ , red line:  $t = 1.213T_c$ , purple line:  $t = 1.222T_c$ , green line:  $t = 1.238T_c$ , blue line:  $t = 1.254T_c$ , yellow line:  $t = 1.27T_c$ , dark red line:  $t = 1.286T_c$ .

maximum pressure reaching up to  $450p_{inf}$  [1.196 $T_c$ , Fig. 20(a)]. Afterward, the peak pressure declines quickly to about  $60p_{inf}$  [1.206 $T_c$ , Fig. 20(b)], which is still higher than the leftmost pressure peak. As the pressure wave propagating away from the shock impacting site, a low-pressure region is formed. Finally, the left moving pressure shock collides with the solid wall, leading to high wall pressure up to about  $21p_{inf}$ .

From the numerical results in Fig. 20, we can find that the shock away from the solid wall can give rise to tremendous pressure pulse, even though it has little influence on the planar solid wall. However, this pressure pulse may lead to the structure damage in the opposite direction. The great dissipations of the shock wave in the liquid are also observed; thus, the impacting strength of the shock on the solid wall depends strongly on the initial stand-off distance.

#### D. Influence of initial stand-off distance on wall pressure

In this subsection, the effect of the initial stand-off distances (from the bubble center to the solid wall) on maximum wall pressure is investigated. Specifically, case studies with initial stand-off distances  $H_0 = 1.1R_0, 1.3R_0, 1.5R_0, 1.7R_0, 2.0R_0,$  and  $2.5R_0$  are performed using present AMR solver.

By placing a pressure probe on the centroid of the planar wall, time history of the wall pressure for the above-mentioned cases is given in Fig. 21. It is found that although the initial stand-off distances are different, the first pressure peaks induced by the shock impacting are always higher than the second peaks induced by the re-entrant jet, which further confirms that the water-hammer shocks is more destructive than the re-entrant jet. Also, we note that the initial stand-off distances have significant influence on the peak wall pressure. When  $H_0 < 2.0R_0$ , the pressure peaks change substantially with respect to the variations of the initial stand-off distance. In particular, for  $H_0 = 1.1R_0$  case (the gap between the bubble front and wall is  $0.1R_0$ ), the magnitude of the first pressure peak reaches  $63p_{inf}$ , which is much higher than the subsequent pressure peak ( $38p_{inf}$ ) caused by re-entrant jet. For  $H_0 = 1.3R_0$  case, the first pressure peak reaches  $35p_{inf}$ , and the second reduces to  $19p_{inf}$ . When  $H_0 = 1.5R_0$ , the first

pressure peak reaches  $21p_{inf}$ , and the second declines to  $12p_{inf}$ . For  $H_0 = 2.5R_0$  case, the shock wave still causes high pressure on the wall with the first pressure peak up to  $8p_{inf}$ . It is also observed that the first pressure peak appears approximately at a similar instant for  $H_0 = 1.1R_0, 1.3R_0, 1.5R_0,$  and  $1.7R_0$  cases, while the second pressure peak occurs at different times. Since the pressure wave toward planar wall dissipates quickly (Fig. 20), the intensity of the wall pressure will be affected greatly by the initial stand-off distance. We may infer that the shock wave propagates with extremely high speed comparable to the speed of sound in liquid. However, the flow speed of re-entrant jet is much lower. Thus, a visible phase differences are expected for the second pressure peaks of various  $H_0$ . In Fig. 21, the obvious delay of the second pressure peaks is found for the six cases; moreover, the values of the second peak pressure decrease significantly with the increase in initial stand-off distance. We notice that when the initial stand-off distances  $H_0 < 2.0R_0$ , the wall pressure oscillates violently after the re-entrant jet impacting, while for  $H_0 = 2.5R_0$ , the pressure curve is relatively smooth (Fig. 21). To identify the sources of the pressure oscillation, bubble dynamic behaviors during collapse are investigated.

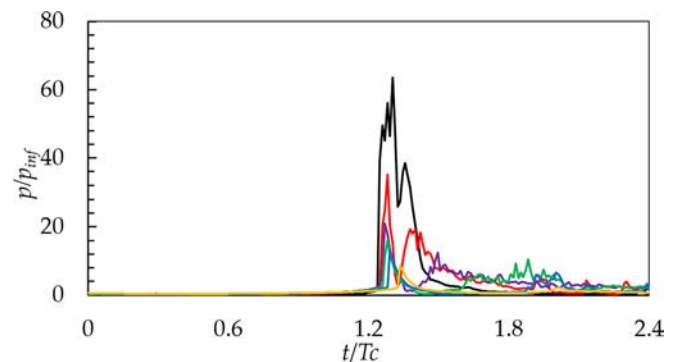


**FIG. 21.** Time history of the wall pressure at the wall center  $[x, y, z] = [0.0, 6.2, 6.2]$  for the different initial stand-off distances. Black line:  $1.1R_0$ , red line:  $1.3R_0$ , purple line:  $1.5R_0$ , green line:  $1.7R_0$ , blue line:  $2.0R_0$ , yellow line:  $2.5R_0$ .

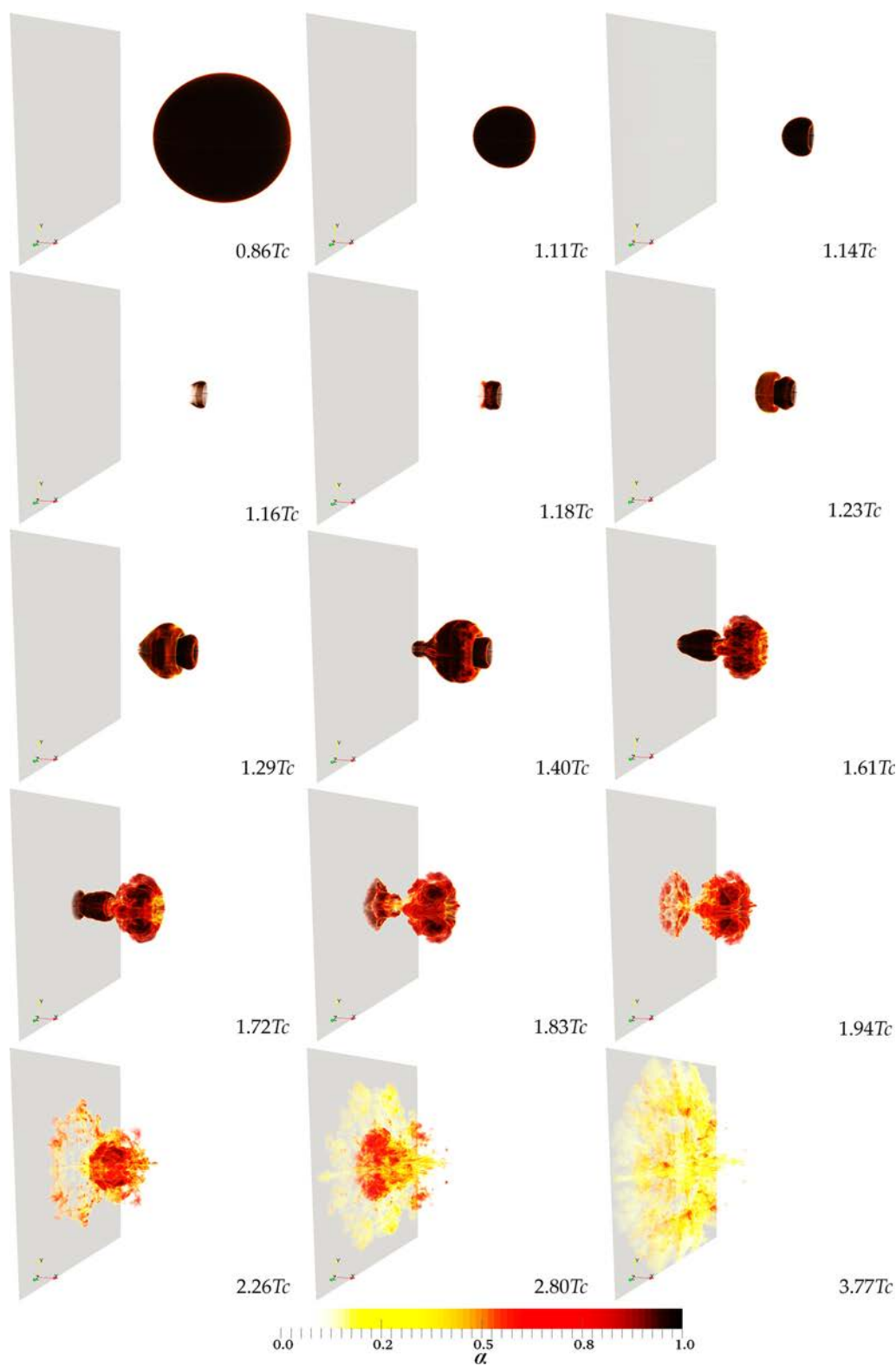


FIG. 22. Evolution of a collapsing bubble with initial stand-off distance of  $1.7R_0$  (rendered by volume fraction).

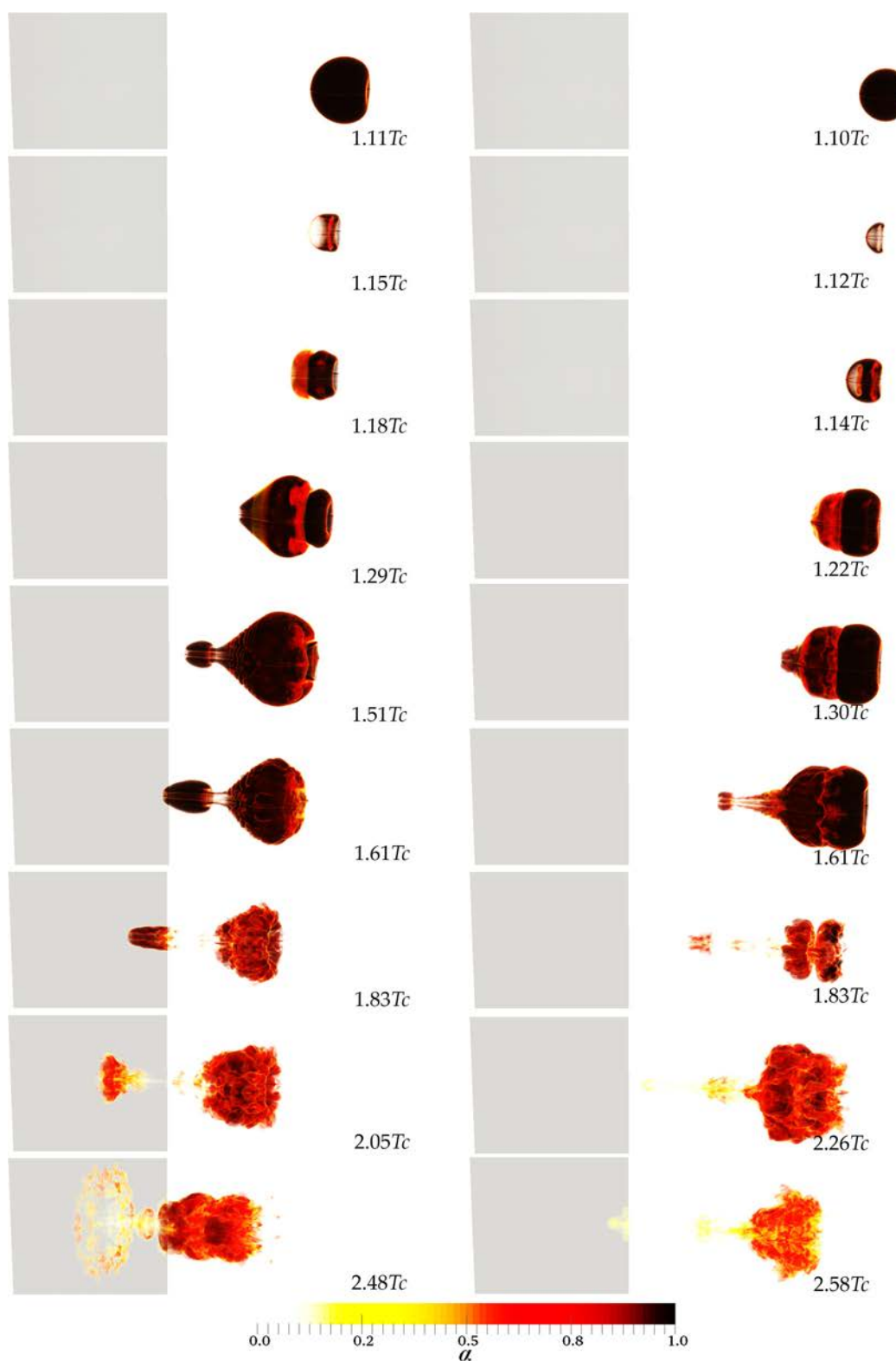


FIG. 23. Evolution of a collapsing bubble in the later stage with initial stand-off distance of  $2.0R_0$  in the left row,  $2.5R_0$  in the right row (rendered by volume fraction).

Figure 22 presents a sequence of snapshots to illustrate the typical dynamics of a collapsing bubble with initial stand-off distance  $H_0 = 1.7R_0$ . In the initial stage, the bubble contracts gradually to become an elliptical shape. Driven by the high pressure difference, the distal side of bubble is flattened at  $1.11Tc$ . Shortly afterward, a visible inward deformation on the distal side of bubble is observed ( $1.14Tc$ ). As the development of shrinking-induced deformation, the distal side evolves into a re-entrant jet impacting onto the proximal side of bubble, followed by the formulation of a toroidal bubble at  $1.18Tc$ . Thereafter, the highly compressed bubble rebounds rapidly at the tip region, with the formation of a mushroom-shape bubble at  $1.29Tc$ . As the bubble moves toward the solid wall, a protrusion induced by the re-entrant jet flow appears ( $1.40Tc$ ); meanwhile, the bubble surface becomes slightly ruffled. The protrusion bubble separates from the toroidal bubble and subsequently collides with the solid wall at  $1.72Tc$ . In the final stages of collapsing ( $1.83Tc$ ,  $1.94Tc$ ), the toroidal bubble breaks up with turbulent jet flow propagates radially along the wall.

Split bubble often has significant influence on the magnitude of wall pressure, and Tong's experimental results<sup>66</sup> suggest that the breakup of the toroidal bubble onto the solid wall may give rise to the wall pressure, which is higher than the shock induced pressure. A successive impingement of the split bubbles (Fig. 22,  $1.72Tc$ – $3.77Tc$ ) accounts for the pressure oscillations partly in the stage of final collapsing (Fig. 21).

Figure 23 presents the collapse patterns with initial stand-off distance  $H_0 = 2.0R_0$ ,  $2.5R_0$ . For  $H_0 = 2.0R_0$  case, the bubble behaviors (i.e., the re-entrant jet, the mushroom-like shape, the protrusion bubble) are similar to  $H_0 = 1.7R_0$  case. However, it is shown that a smaller protrusion bubble is formed and impacts the wall. In addition, the bubble left in liquid does not contact with the solid wall eventually.

For  $H_0 = 2.5R_0$  case, bubble is developed with significant differences compared with previous two cases ( $H_0 = 1.7R_0$  and  $2.0R_0$ ). After the bubble splits into two parts at the rebounding stage, the split part in left side forms a much smaller protrusion shape bubble ( $1.3Tc$ ), a gourd-shape, rather than a mushroom-shape bubble emerged. Compared with  $H_0 = 2.0R_0$  case, a smaller bubble is detached from the protrusion bubble and moving toward the solid wall ( $1.61Tc$ ). The remnant part re-collapses and splits into two bubbles at  $1.83Tc$ , followed by re-expansion and coalescence. The expansion–contraction process will repeat until the pressure in- and outside the bubble reaches equilibrium. Due to the larger stand-off distance, the split bubbles do not contact the solid wall finally; thus, a smoother pressure variation is shown for  $H_0 = 2.5R_0$  case (Fig. 21).

## V. CONCLUSIONS

In this study, a compressible two-phase flow solver is developed to simulate the collapsing process of a single air bubble in water. The highly robust wave propagation method with Riemann solver (HLLC) is applied to solve the five-equation model. The WENO scheme with block-structured AMR method is adopted to reduce the numerical dissipation and improve the computational efficiency. From the convergence analysis, excellent agreement is found between the predicted results (bubble radius and pressure as function of time) and the theoretical solutions (K–M theory). We perform a comprehensive and quantitative analysis to investigate the formation of shock waves in a collapsing bubble and the pressure acting on planar solid wall, with the following conclusions:

- (1) It can be concluded that the piston-like motion of the re-entrant jet leads to the generation of shock wave inside bubble. The shock is refracted at the bubble interface, forming a precursor transmitted shock propagating into liquid and a reflected shock inside bubble. Eventually, the reflected shock impacts the tip of the re-entrant jet, resulting in an enhanced water-hammer shock in the liquid.
- (2) It is found that the water-hammer shock will merge with the precursor shock and give rise to the first peak of wall pressure. Although the strength of the merged-shock dissipated rapidly, the wall pressure induced by water-hammer shock still shows much higher magnitude than the pressure generated by the re-entrant jet only. Thus, we can conclude that shock waves are the primary reason for the cavitation damage.
- (3) We found that the water-hammer shock traveling opposite to the wall causes tremendous pressure pulse. It occurs when the water-hammer shock approaches the reflected shock in the distal side of the bubble. The enhanced shock–shock interaction results in a drastic increase in pressure, up to  $450p_{inf}$  [Fig. 20(a)].
- (4) The initial stand-off distance is a key factor on the wall pressure peak and bubble dynamic behaviors. For  $H_0 \geq 2.5R_0$ , the re-entrant jet cannot contact with wall, but the shock wave still produces high pressure on the wall. When  $H_0 \leq 2.5R_0$ , rebounding occurs at the bubble tip region, and a typical mushroom-shape bubble ( $H_0 = 1.7R_0$ ,  $2.0R_0$ ) or a gourd-shape bubble ( $H_0 = 2.5R_0$ ) will be produced. As there is an increase of  $H_0$ , the size of the protrusion bubble split from the toroidal bubble declines. The protrusion bubble and the remnant part impacts the wall successively, giving rise to the oscillations of wall pressure in the final stage of the collapse.

## ACKNOWLEDGMENTS

This work was supported by the National Natural Science Foundation of China (Grant Nos. 51979160 and 11902199), Shanghai Pujiang Talent Program (Grant No. 19PJ1406100), and National Key Research and Development Program of China (Grant Nos. 2019YFB1704200 and 2019YFC0312400), to which the authors are most grateful.

## DATA AVAILABILITY

The data that support the findings of this study are available from the corresponding author upon reasonable request.

## REFERENCES

- <sup>1</sup>L. Rayleigh, "VIII. On the pressure developed in a liquid during the collapse of a spherical cavity," *London, Edinburgh, Dublin Philos. Mag. J. Sci.* **34**(200), 94–98 (1917).
- <sup>2</sup>S. R. Gonzalez-Avila, F. Denner, and C.-D. Ohl, "The acoustic pressure generated by the cavitation bubble expansion and collapse near a rigid wall," *Phys. Fluids* **33**(3), 032118 (2021).
- <sup>3</sup>M. Kornfeld and L. Suvorov, "On the destructive action of cavitation," *J. Appl. Phys.* **15**(6), 495–506 (1944).
- <sup>4</sup>M. Rattray, *Perturbation Effects in Cavitation Bubble Dynamics* (California Institute of Technology, 1951).
- <sup>5</sup>T. B. Benjamin and A. T. Ellis, "The collapse of cavitation bubbles and the pressures thereby produced against solid boundaries," *Philos. Trans. R. Soc., A* **260**, 221–240 (1966).

- <sup>6</sup>L. Liu, X. Yao, A. Zhang *et al.*, “Numerical analysis of the jet stage of bubble near a solid wall using a front tracking method,” *Phys. Fluids* **29**(1), 012105 (2017).
- <sup>7</sup>N. D. Shutler and R. B. Mesler, “A photographic study of the dynamics and damage capabilities of bubbles collapsing near solid boundaries,” *J. Basic Eng.* **87**(2), 511–517 (1965).
- <sup>8</sup>A. Shima, K. Takayama, Y. Tomita *et al.*, “Mechanism of impact pressure generation from spark-generated bubble collapse near a wall,” *AIAA J.* **21**(1), 55–59 (1983).
- <sup>9</sup>Y. Tomita and A. Shima, “Mechanisms of impulsive pressure generation and damage pit formation by bubble collapse,” *J. Fluid Mech.* **169**, 535–564 (1986).
- <sup>10</sup>G. Huang, M. Zhang, X. Ma *et al.*, “Dynamic behavior of a single bubble between the free surface and rigid wall,” *Ultrason. Sonochem.* **67**, 105147 (2020).
- <sup>11</sup>A. Zhang, P. Cui, and Y. Wang, “Experiments on bubble dynamics between a free surface and a rigid wall,” *Exp. Fluids* **54**(10), 1602 (2013).
- <sup>12</sup>D. Kim and D. Kim, “Underwater bubble collapse on a ridge-patterned structure,” *Phys. Fluids* **32**(5), 053312 (2020).
- <sup>13</sup>W. Lauterborn and H. Bolle, “Experimental investigations of cavitation-bubble collapse in the neighbourhood of a solid boundary,” *J. Fluid Mech.* **72**(2), 391–399 (1975).
- <sup>14</sup>W. Lauterborn, *Cavitation Bubble Dynamics—New Tools for an Intricate Problem, Mechanics and Physics of Bubbles in Liquids* (Springer, 1982), pp. 165–178.
- <sup>15</sup>Y. Tomita and T. Kodama, “Interaction of laser-induced cavitation bubbles with composite surfaces,” *J. Appl. Phys.* **94**(5), 2809–2816 (2003).
- <sup>16</sup>Y. X. Yang, Q. X. Wang, and T. Keat, “Dynamic features of a laser-induced cavitation bubble near a solid boundary,” *Ultrason. Sonochem.* **20**(4), 1098–1103 (2013).
- <sup>17</sup>F. Reuter and S. A. Kaiser, “High-speed film-thickness measurements between a collapsing cavitation bubble and a solid surface with total internal reflection shadowmetry,” *Phys. Fluids* **31**(9), 097108 (2019).
- <sup>18</sup>V. Robles, E. Gutierrez-Herrera, L. F. Devia-Cruz *et al.*, “Soft material perforation via double-bubble laser-induced cavitation microjets,” *Phys. Fluids* **32**(4), 042005 (2020).
- <sup>19</sup>M. S. Plesset, “The dynamics of cavitation bubbles,” *J. Appl. Mech.* **16**, 277–282 (1949).
- <sup>20</sup>J. B. Keller and M. Miksis, “Bubble oscillations of large amplitude,” *J. Acoust. Soc. Am.* **68**(2), 628–633 (1980).
- <sup>21</sup>A. Tiwari, J. B. Freund, and C. Pantano, “A diffuse interface model with immiscibility preservation,” *J. Comput. Phys.* **252**, 290–309 (2013).
- <sup>22</sup>S. Beig, B. Aboulhasanzadeh, and E. Johnsen, “Temperatures produced by inertially collapsing bubbles near rigid surfaces,” *J. Fluid Mech.* **852**, 105–125 (2018).
- <sup>23</sup>K. Schmidmayer, S. H. Bryngelson, and T. Colonius, “An assessment of multi-component flow models and interface capturing schemes for spherical bubble dynamics,” *J. Comput. Phys.* **402**, 109080 (2020).
- <sup>24</sup>C. Lechner, M. Koch, W. Lauterborn *et al.*, “Pressure and tension waves from bubble collapse near a solid boundary: A numerical approach,” *J. Acoust. Soc. Am.* **142**(6), 3649–3659 (2017).
- <sup>25</sup>M. S. Plesset and R. B. Chapman, “Collapse of an initially spherical vapour cavity in the neighbourhood of a solid boundary,” *J. Fluid Mech.* **47**(2), 283–290 (1971).
- <sup>26</sup>J. R. Blake and D. Gibson, “Growth and collapse of a vapour cavity near a free surface,” *J. Fluid Mech.* **111**, 123–140 (1981).
- <sup>27</sup>A. Pearson, E. Cox, J. Blake *et al.*, “Bubble interactions near a free surface,” *Eng. Anal. Boundary Elem.* **28**(4), 295–313 (2004).
- <sup>28</sup>S. Li, Y.-B. Li, and A.-M. Zhang, “Numerical analysis of the bubble jet impact on a rigid wall,” *Appl. Ocean Res.* **50**, 227–236 (2015).
- <sup>29</sup>L. Liu, X. Yao, A. Zhang *et al.*, “Research on the estimate formulas for underwater explosion bubble jet parameters,” *Ocean Eng.* **164**, 563–576 (2018).
- <sup>30</sup>S. Li, A.-M. Zhang, R. Han *et al.*, “Experimental and numerical study of two underwater explosion bubbles: Coalescence, fragmentation and shock wave emission,” *Ocean Eng.* **190**, 106414 (2019).
- <sup>31</sup>R. Han, A.-M. Zhang, S. Li *et al.*, “Experimental and numerical study of the effects of a wall on the coalescence and collapse of bubble pairs,” *Phys. Fluids* **30**(4), 042107 (2018).
- <sup>32</sup>R. Han, L. Tao, A.-M. Zhang *et al.*, “A three-dimensional modeling for coalescence of multiple cavitation bubbles near a rigid wall,” *Phys. Fluids* **31**(6), 062107 (2019).
- <sup>33</sup>C. Liu and C. Hu, “Adaptive THINC-GFM for compressible multi-medium flows,” *J. Comput. Phys.* **342**, 43–65 (2017).
- <sup>34</sup>F. Xiao, Y. Honma, and T. Kono, “A simple algebraic interface capturing scheme using hyperbolic tangent function,” *Int. J. Numer. Methods Fluids* **48**(9), 1023–1040 (2005).
- <sup>35</sup>R. P. Fedkiw, T. Aslam, B. Merriman *et al.*, “A non-oscillatory Eulerian approach to interfaces in multimaterial flows (the ghost fluid method),” *J. Comput. Phys.* **152**(2), 457–492 (1999).
- <sup>36</sup>G. Allaire, S. Clerc, and S. Kokh, “A five-equation model for the simulation of interfaces between compressible fluids,” *J. Comput. Phys.* **181**(2), 577–616 (2002).
- <sup>37</sup>X. Deng, S. Inaba, B. Xie *et al.*, “High fidelity discontinuity-resolving reconstruction for compressible multiphase flows with moving interfaces,” *J. Comput. Phys.* **371**, 945–966 (2018).
- <sup>38</sup>A. K. Kapila, R. Menikoff, J. B. Dzil *et al.*, “Two-phase modeling of deflagration-to-detonation transition in granular materials: Reduced equations,” *Phys. Fluids* **13**(10), 3002–3024 (2001).
- <sup>39</sup>M. Baer and J. Nunziato, “A two-phase mixture theory for the deflagration-to-detonation transition (DDT) in reactive granular materials,” *Int. J. Multiphase Flow* **12**(6), 861–889 (1986).
- <sup>40</sup>R. Saurel, F. Petitpas, and R. A. Berry, “Simple and efficient relaxation methods for interfaces separating compressible fluids, cavitating flows and shocks in multiphase mixtures,” *J. Comput. Phys.* **228**(5), 1678–1712 (2009).
- <sup>41</sup>S. Shaw and P. Speltz, “Shock emission from collapsing gas bubbles,” *J. Fluid Mech.* **646**, 363 (2010).
- <sup>42</sup>E. Johnsen and T. Colonius, W. Kreider *et al.*, “Non-spherical collapse of an air bubble subjected to a lithotripter pulse,” in *Proceedings of ASME International Mechanical Engineering Congress and Exposition* (ASME, 2007), pp. 285–294.
- <sup>43</sup>E. Johnsen and T. Colonius, “Shock-induced collapse of a gas bubble in shock-wave lithotripsy,” *J. Acoust. Soc. Am.* **124**(4), 2011–2020 (2008).
- <sup>44</sup>E. Johnsen and T. Colonius, “Numerical simulations of non-spherical bubble collapse,” *J. Fluid Mech.* **629**, 231 (2009).
- <sup>45</sup>K.-M. Shyue, “An efficient shock-capturing algorithm for compressible multi-component problems,” *J. Comput. Phys.* **142**(1), 208–242 (1998).
- <sup>46</sup>C.-T. Hsiao, A. Jayaprakash, A. Kapahi *et al.*, “Modelling of material pitting from cavitation bubble collapse,” *J. Fluid Mech.* **755**, 142–175 (2014).
- <sup>47</sup>Z.-L. Tian, A.-M. Zhang, Y.-L. Liu *et al.*, “A new 3-D multi-fluid model with the application in bubble dynamics using the adaptive mesh refinement,” *Ocean Eng.* **230**, 108989 (2021).
- <sup>48</sup>T. Trummer, S. J. Schmidt, and N. A. Adams, “Effect of stand-off distance and spatial resolution on the pressure impact of near-wall vapor bubble collapses,” *Int. J. Multiphase Flow* **141**, 103618 (2021).
- <sup>49</sup>K. Johansen, J. H. Song, K. Johnston *et al.*, “Deconvolution of acoustically detected bubble-collapse shock waves,” *Ultrasonics* **73**, 144–153 (2017).
- <sup>50</sup>Z.-L. Tian, Y.-L. Liu, A.-M. Zhang *et al.*, “Jet development and impact load of underwater explosion bubble on solid wall,” *Appl. Ocean Res.* **95**, 102013 (2020).
- <sup>51</sup>S. Cao, G. Wang, O. Coutier-Delgosha *et al.*, “Shock-induced bubble collapse near solid materials: Effect of acoustic impedance,” *J. Fluid Mech.* **907**, A17 (2021).
- <sup>52</sup>C. Lechner, W. Lauterborn, M. Koch *et al.*, “Fast, thin jets from bubbles expanding and collapsing in extreme vicinity to a solid boundary: A numerical study,” *Phys. Rev. Fluids* **4**(2), 021601(R) (2019).
- <sup>53</sup>G.-S. Jiang and C.-W. Shu, “Efficient implementation of weighted ENO schemes,” *J. Comput. Phys.* **126**(1), 202–228 (1996).
- <sup>54</sup>A. Murrone and H. Guillard, “A five equation reduced model for compressible two phase flow problems,” *J. Comput. Phys.* **202**(2), 664–698 (2005).
- <sup>55</sup>R. Menikoff and B. J. Plohr, “The Riemann problem for fluid flow of real materials,” *Rev. Mod. Phys.* **61**(1), 75 (1989).
- <sup>56</sup>V. Coralic and T. Colonius, “Finite-volume WENO scheme for viscous compressible multicomponent flows,” *J. Comput. Phys.* **274**, 95–121 (2014).

- <sup>57</sup>D. P. Garrick, M. Owkes, and J. D. Regele, “A finite-volume HLLC-based scheme for compressible interfacial flows with surface tension,” *J. Comput. Phys.* **339**, 46–67 (2017).
- <sup>58</sup>D. I. Ketcheson, M. Parsani, and R. J. Leveque, “High-order wave propagation algorithms for hyperbolic systems,” *SIAM J. Sci. Comput.* **35**(1), A351–A377 (2013).
- <sup>59</sup>E. F. Toro, *Riemann Solvers and Numerical Methods for Fluid Dynamics: A Practical Introduction* (Springer Science & Business Media, 2009).
- <sup>60</sup>X. Zhang and C.-W. Shu, “Maximum-principle-satisfying and positivity-preserving high-order schemes for conservation laws: Survey and new developments,” *Proc. R. Soc. A* **467**(2134), 2752–2776 (2011).
- <sup>61</sup>M. J. Berger and J. Olinger, “Adaptive mesh refinement for hyperbolic partial differential equations,” *J. Comput. Phys.* **53**(3), 484–512 (1984).
- <sup>62</sup>P. Macneice, K. M. Olson, C. Mobarry *et al.*, “PARAMESH: A parallel adaptive mesh refinement community toolkit,” *Comput. Phys. Commun.* **126**(3), 330–354 (2000).
- <sup>63</sup>C. Liu and C. Hu, “An adaptive multi-moment FVM approach for incompressible flows,” *J. Comput. Phys.* **359**, 239–262 (2018).
- <sup>64</sup>C. D. Ohl, T. Kurz, R. Geisler *et al.*, “Bubble dynamics, shock waves and sonoluminescence,” *Philos. Trans. R. Soc., A* **357**(1751), 269–294 (1999).
- <sup>65</sup>O. Lindau and W. Lauterborn, “Cinematographic observation of the collapse and rebound of a laser-produced cavitation bubble near a wall,” *J. Fluid Mech.* **479**, 327 (2003).
- <sup>66</sup>R. Tong, W. P. Schiffers, S. J. Shaw *et al.*, “The role of ‘splashing’ in the collapse of a laser-generated cavity near a rigid boundary,” *J. Fluid Mech.* **380**, 339–361 (1999).